PERFORMANCE AND SOLUBILITY STUDIES OF IRON-BASED COMPLEX FOR REDOX FLOW BATTERIES

A Thesis

by

Huyen Thanh Bui

BS, Texas A&M University-Corpus Christi, 2019

Submitted in Partial Fulfillment of the Requirements for the Degree of

MASTER OF SCIENCE

in

CHEMISTRY

Texas A&M University-Corpus Christi
Corpus Christi, Texas

August 2021

August 2021

PERFORMANCE AND SOLUBILITY STUDIES OF AN IRON-BASED COMPLEX FOR REDOX FLOW BATTERIES

A Thesis

by

HUYEN THANH BUI

This thesis meets the standards for scope and quality of
Texas A&M University-Corpus Christi and is hereby approved.

Nicolas Holubowitch, PhD
Chair

Jai Prakash, PhD
Committee Member

Iltai Isaac Kim, PhD
Committee Member

August 2021

ABSTRACT

Although renewable energy, such as wind or solar panels, is advancing very fast nowadays, energy storage is still an unsolved problem to making renewable energy economically competitive with fossil fuel-based energy. Redox flow batteries (RFBs), which are emerging electrochemical technologies for large scale energy storage, are a promising solution. They have a simple design, high energy efficiency and are eco-friendly but are too expensive with currently used materials (typically vanadium). This research aims to synthesize and investigate the viability of inexpensive iron-based compounds for RFBs, in order to improve their output voltage, energy density, and lifetime.

A major challenge with RFBs in general and Iron (Fe)-complexes specifically is achieving high solubility of the active compound to give a battery with high energy density. This work explores options such as additives and alternative supporting electrolytes to increase the aqueous solubility of Tris(bipyridyl) Iron complexes ($Fe(bpy)_3SO_4$) and related active RFB compounds. The solubility was studied based on the absorbance of Iron complexes solution combined with different additives. The results show that Isopropyl alcohol (IPA) can increase the solubility of $Fe(bpy)_3SO_4$ in RFB electrolytes from ~ 0.1M to 0.35M. Multiple instruments will be used to investigate the iron-based compound's electrochemical characteristics and suitability for RFBs (including effects of the additive). The Rotating Disk Electrode will be used to study the iron-based compound's redox behavior and kinetics study, such as: redox potentials via cyclic voltammetry, linear sweep voltammetry, diffusion coefficient, electrons transfer rate constants, etc. In addition, the compound's battery performance in full, lab-scale redox flow batteries will be tested with the novel high – concentration solution of the iron compound to determine its capacity and check for degradation. Moreover, the side reaction of $Fe(bpy)_3SO_4$, which is dimerization that

sacrifices battery voltage, also was studied in this project. It is important to minimize the dimerization in order to avoid voltage efficiency loss during cycling. Ultimately, a new RFB composed of 2,7- anthraquinone disulfonic acid disodium salt anolyte and the solubility-enhanced iron – complex catholyte was constructed and put through a variety of operational tests including long-term performance for over 200 cycles. This new battery design operates under mild conditions with all earth-abundant elements and is a promising candidate for grid-scale energy storage.

ACKNOWLEDGEMENTS

Completing a Master's degree is an important task of my life and it is unforgettable experience. To make this far, I received a lot of supports from my friends, my lab partner, my supervisor, and my family.

I own many thanks to my supervisor, Dr. Nicolas Holubowitch, who has a huge contribution to my project. Thank you for your patient, support, and guidance over 3 years since I was in undergraduate student. It was my honest to have worked with Dr. Nicolas Holubowitch. I could not go through it without his advice and guide that I will never forget. Thank you for giving me many research ideas, teaching me, develop my research, and especially revising my thesis.

I extend my appreciation to my committee, Dr. Iltai Isaac Kim and Dr. Jai Prakash, for their advice and editing my thesis. They are outstanding and have a wonderful guidance. I also want to thank Dr. Fereshteh Billiot for her kind, helpful assistance, and encouragement. She gave me a lot of instruction and suggestion when I meet challenges. Special thanks also go to my lab partner, Giang Nguyen, for her encouragement and help me develop my thesis. I do enjoy all the time that we have discussion and work together. Furthermore, I would like to thank my colleagues, Uyen Le, Ha Tran and Vu Nguyen, for their support and assistance on my thesis.

Last but not the least, I would like to thank my family. My grandparents, my uncle, my aunt, and especially my parents are always encouraging and support me. My parents are always support me throughout my life and stay by my side. I am very grateful for their love, caring and sacrifices for my future. Thank you for everything.

TABLE OF CONTENTS

LIST OF FIGURES

FIGURES PAGE

LIST OF TABLES

TABLES PAGE

CHAPTER I – INTRODUCTION

1.1. Background

Since the global population is increasing rapidly, it is necessary to improve the electricity supply due to the high demand. There are three main sources of electricity generation: combustion of fossil fuel, nuclear energy and renewable energy. Most of the electricity worldwide (68%) is generated from fossil fuels, which include coal, natural gas, and oil [1]. However, generated electricity from fossil fuel causes a huge amount of carbon dioxide emissions that lead to environmental pollution. Moreover, to produce coal, gas and oil, we must dig deep to the surface of the Earth, which has negative environment consequences. Nuclear energy offers a better electricity generation option in terms of low carbon emissions and long – term output; however, Earth has limited radioactive resources that are difficult to obtain and purify and nuclear waste poses an enormous hazard for the future of mankind [2]. Renewable energy sources such as wind, solar, geothermal and tidal energies are abundant. They are eco-friendly, potentially inexpensive, and can theoretically satisfy the high demand of electricity. However, the biggest issue of renewable energy compared to the others is their inconstancy; thus energy storage is required to utilize their energy output 24 hours a day. Meanwhile fossil fuel and nuclear energy are always available and easy to be stored and deliver s constant energy output; renewable energy is often dependent on weather and the excess energy produced during good weather is rarely stored for later use. Redox Flow Batteries (RFBs) are one of the solutions that can solve this problem. It is considered as one of the best and safest options for long duration discharge at relatively low cost.

Table 1. show the advantages and disadvantages of RFBs compare to Lithium-ion Batteries, a well-established battery technology that is also being considered for large-scale energy

storage. The major advantage of RFBs is that the electrolyte and electroactive materials are stored externally, which separate the power output and energy capacity [3][4]. The battery stack and electrolyte tanks can be built as big as they are needed for a specific renewable energy farm. In contrast, Lithium-ion and other metal batteries are sealed with inflexible power and energy delivery. However, the main disadvantage of RFB is the requirement of moving parts such as pumps, vessels, sensors, etc. to build up a compatible system for utility scale which leads to potentially high maintenance costs [3]. Nevertheless, RFBs are expected to be more stable and durable than Lithium-ion batteries since the electrodes do not undergo any physical or chemical degradation [3]. Another benefit of RFBs is their active components, which can be safe and friendly to the environment. The electroactive materials of RFB are easier to make and find without mining costly metals. Thus, RFBs have potentially lower costs compare to Lithium-ion batteries. Furthermore, Lithium-ion Batteries require a high protection system due to high risk of fires since they use highly flammable materials. Currently, although Lithium-ion batteries has many disadvantages, it still has higher power density and energy compare to RFB, however lower energy density but safe batteries could be acceptable in the large areas available at renewable energy generation and storage sites [4]. The Department of Energy has set a cost target for energy storage systems of $150/kWh by 2023 [5].

	Redox Flow Batteries	Lithium-ion Batteries
Design and construction	External (scalable electrolyte tanks)	Internal (completely sealed)
Components	Require pump, vessel, sensors, etc. Require membrane Eco-friendly, safe	Rare metals like Co, Ni, Li Organic solvent Require high protection
Performance	More stable and durable Low voltage output (aqueous systems)	Less stable and durable High voltage (non-aqueous)
Flammable	No	Yes
Power density	Low	High
Cost	Low	High

Table 1. Advantages and disadvantages comparison between RFB and Lithium-ion Batteries.

1.2. Design and construction

Redox flow batteries (RFBs) are electrochemical energy storage devices [5] that function as secondary (rechargeable) batteries designed with two tanks containing anolyte and catholyte liquids, which are pumped into the battery during operation where they are separated by a membrane (Figure 1.1). As mentioned above, RFBs do not undergo an intercalation mechanism, which leads to materials degradation in Li-ion batteries; all active materials remain soluble in the

electrolytes. The anolyte or catholyte are the battery's active electrochemical species and can be inorganic, organic, or organometallic compounds that serve as anode and cathode materials dissolved in the electrolyte solutions. When charging a battery, the catholyte is the source of positive charge or electron donor. The process of oxidation occurs in the cathode during charge state. In contrast, anolyte is the source of electrons or electron acceptor. Active molecules are reduced at the catholyte during discharge and accept electrons from the external circuit. A membrane serves as a salt-bridge type barrier, where ions freely move between catholyte to anolyte and serve to separate the solutions and balance charge, but prevents electrolyte mixing and internal electron flow.

Many research focus on non-aqueous RFBs nowadays due to the promising of high energy density; but it has same issues, which is flammable, as Li-ion battery. Thus, this research is focused on aqueous RFBs. To improve the power density of aqueous RFBs, many aspects are being investigated such as supporting electrolyte, membrane, and new redox species (Figure 1.2). There is much research into electroactive compounds for redox flow batteries and some technologies have been commercialized such as vanadium, polysulfide bromide and inorganic iron. However, these chemistries still suffer from high cost, toxicity, stability, and/or high degradation rates with cycling [7][8]. All-organic compounds such as quinones are being intensively explored as active redox species, however they often suffer from low solubility, complex syntheses, low output voltages and poor long-term stability. Another alternative option includes organometallic complexes such as iron-based chelation complexes, which have attractive properties such as high voltage output, low cost and operation at near neutral pH. In this work, we are interested in investigating and improving the properties of iron polypyridyl complexes as RFB catholyte compounds. Initial studies will focus

on the iron (II/III) tris(2,2'-bipyridine) (Figure 1.3) aka $Fe(bpy)_3^{2+/3+}$ redox couple, which has some very promising properties related to RFBs but also some drawbacks that need to be addressed. This thesis is focused on improving upon those drawbacks which will be described in detail below.

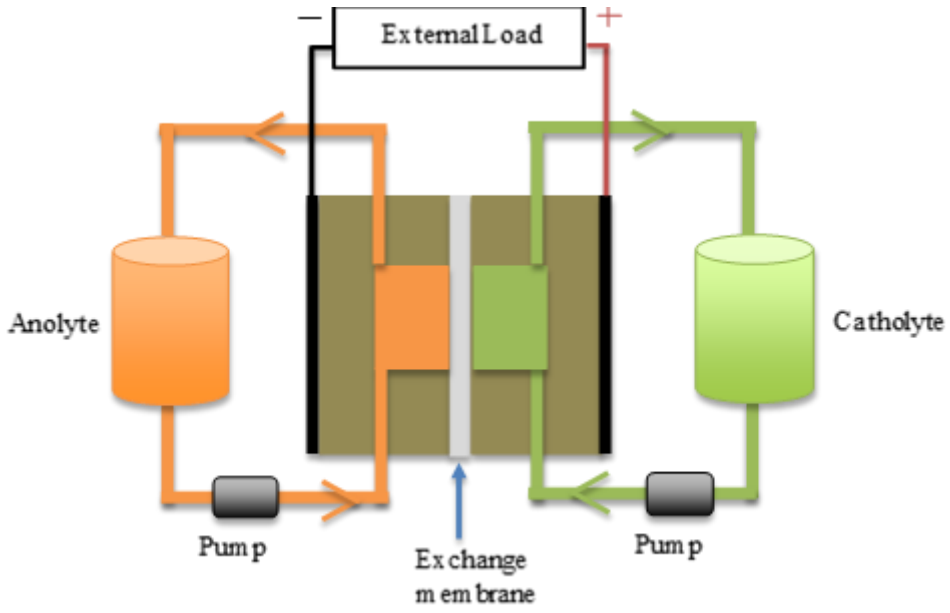

Figure 1.1 Schematic of a typical redox flow battery

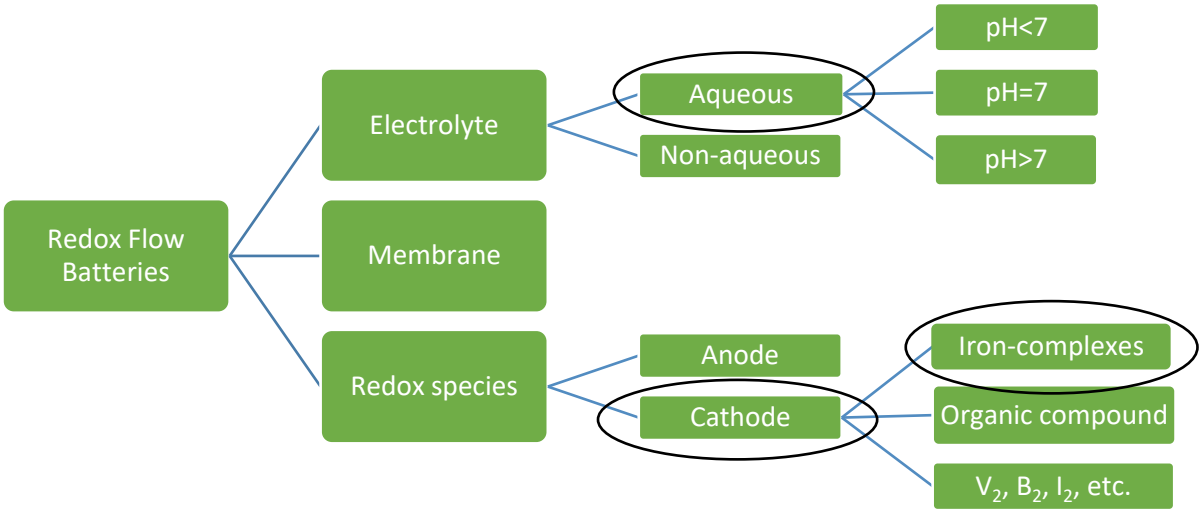

Figure 1.2 Design of Redox Flow Battery

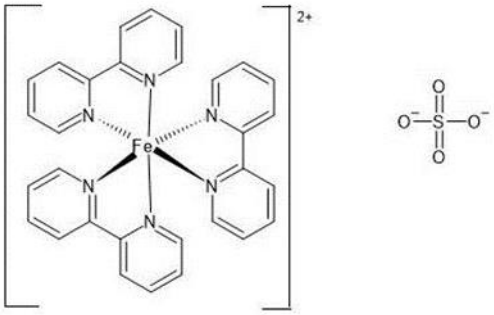

Figure 1.3 Iron (II) tris (2-2'-bipyridine) sulfate

Table 2 summarize some pros and cons of $Fe(bpy)_3SO_4$ as the catholyte for RFB. There are many promising compounds for RFB such as 2,2,6,6-tetramethylpiperidine-1-oxyl (TEMPO), ferrocenes and other organometallic compounds. TEMPO and its derivatives are the attractive candidate for RFBs due to their high potential, rapid charge transfer kinetics and high solubility in water [9]. However, TEMPO and other compounds are expensive, have a big issue with membrane crossover and long-term stability [9]. Besides, $Fe(bpy)_3SO_4$ is built from inexpensive earth – abundant elements and have a high redox potential. It also dissolves in water, which satisfy our requirement, and has simple synthesis. But $Fe(bpy)_3SO_4$ has some issue, which are low solubility, unstable in aqueous solution and low energy. These issues will be discussing later in this thesis.

	$Fe(bpy)_3SO_4$
Pros	Abundant element Ecofriendly, inexpensive High redox potential (1.03 vs SHE) Dissolve in water Simple synthesis
Cons	Low solubility Unstable in aqueous solution Low power and energy density

Table 2. Pros and Cons of $Fe(bpy)_3SO_4$

1.3. Reaction mechanism of Iron-complexes

Much research about the chemistry of 2,2'-bipyridine complexes of Fe(III) and Fe(II) in the past due to its interesting light-absorbing and redox properties. However, specific details of its RFB-related properties and performance, namely solubility and the electrochemical dimerization, have not been established. For further investigation, it is important to understand the electrochemical reactions of this catholyte in a redox flow battery [9]:

Charge:

$$[Fe(bpy)_3]^{2+} \xleftrightarrow{E=1.03V \text{ vs SHE}} [Fe(bpy)_3]^{3+} + e^- \quad (1)$$

(unstable)

$$2[Fe(bpy)_3]^{3+} + 2Cl^- + H_2O \longrightarrow [Fe(bpy)_4OCl_2]^{2+} + 2Hbpy^+ \quad (2)$$

(dimer)

Discharge:

$$[Fe(bpy)_4OCl_2]^{2+} + 2Hbpy^{+} + 2e^{-} \xrightarrow{E=0.35V \text{ vs SHE}} 2[Fe(bpy)_3]^{2+} + 2Cl^{-} + H_2O \quad (3)$$

During the charging process, the strongly red colored $[Fe(bpy)_3]^{2+}$ species is oxidized to a light blew colored $[Fe(bpy)_3]^{3+}$. The redox potential of 1.03 V vs. SHE is very high (near the oxygen evolution potential for water) and thus could produce a high-voltage battery. However, this product is unstable in aqueous solution; turning to the result of reaction (2) where $[Fe(bpy)_3]^{3+}$ slowly reacts with components in the electrolyte solution to form the dimer. To explain for this situation, Fe(III) species is a strong Lewis acid that susceptible to nucleophilic attack by weak base such as water or Cl^-. Further details regarding this complex chemical mechanism can be found elsewhere (Ehman reference) [20].

Recent studies have shown that the charged form of the iron bipyridine complex, i.e. $Fe(bpy)_3^{3+}$, is unstable toward dimerization. if the battery is held in a charged state for any duration of time [9]. Ruan et al. showed (see literature review below) that the 3+ species dimerizes in solution into a lower energy state, leading to a low voltage plateau during discharge, the consequence being lower power output of the battery. The original 2+ form is eventually regenerated so there is no irreversible capacity decay with cycling; however, destabilization of the 3+ species needs to be studied better and perhaps inhibited with additives. The compounds in a charged redox flow battery will need to be stable over many hours or days for them to be commercially viable in load-shifting renewable energies. The other main challenge with $Fe(bpy)_3SO_4$ is its poor solubility in RFB electrolyte (only demonstrated up to 0.1 M in an RFB).

Therefore, this work seeks to study additives that may improve solubility of the active catholyte and investigate their effects on redox performance and charged (3+) species stability.

1.4. Fundamental analysis of electrochemical performance

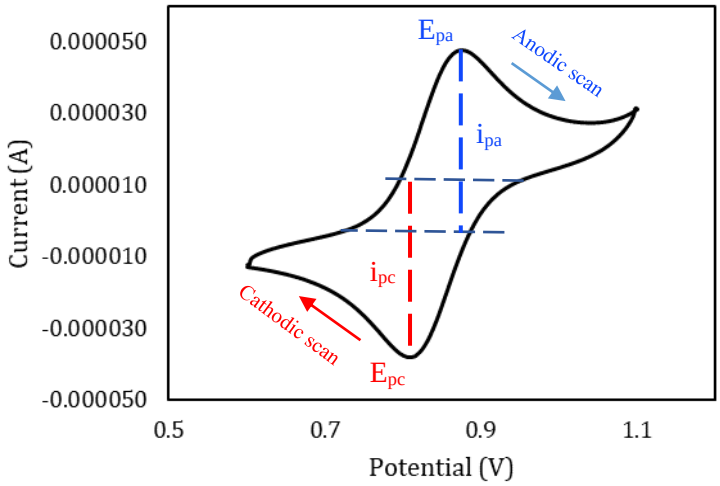

Figure 1.4 An example of the cyclic voltammogram (CV) at a reasonable scan rate. RFB compounds should exhibit reversible redox behavior, indicated by small oxidation/reduction peak separation in CV.

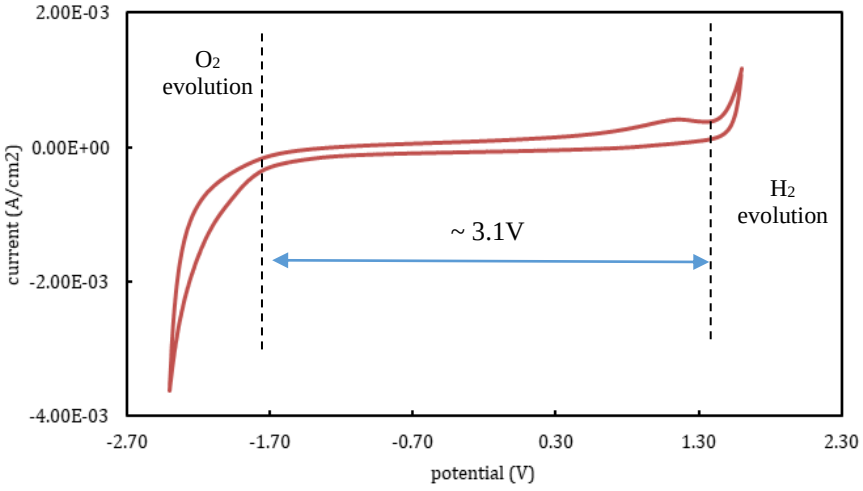

Figure 1.5 Blank cyclic voltammogram of 0.5M NaCl

An electroactive compound for RFBs must have reversible redox behavior. Cyclic voltammetry (CV) is used to determine if possible active compounds show redox reversibility as well as the voltage window of the solvent/supporting electrolyte system. Figure 1.4 is given to show a CV for reversible oxidation/reduction of a generic redox couple. The peaks correspond to current maxima achieved as active species diffuse to the electrode surface and react, followed by stead-state diffusion to the electrode surface at more extreme potentials [10]. A suitable RFB compound (for anolyte or catholyte) should show this type of behavior with small peak splitting and an anodic (i_{pa})/cathodic (i_{pc}) peak current ratio near 1. The anolyte should have redox peaks at as negative potentials as possible (E_{pa}), while the catholyte should have a very high positive redox potential (E_{pc}); these redox events should approach but not overlap with solvent decomposition features. Figure 1.5 illustrate the voltammogram of an electrolyte solution (0.5 M). A suitable redox species for NaCl should has a redox behavior fall into the range of -1.7V -1.3V. It is critical to maximize the difference in redox potentials, $E_{cell} = E_{pc} - E_{pa}$, which determines the RFB's discharging voltage and thus power output and energy density. At the same time, the E_{pa} and E_{pc} potentials must fall within the solvent's (usually water) electrochemical stability window.

Cyclic voltammetry mainly establishes the battery-relevant thermodynamic properties of possible active compounds, while linear sweep voltammetry (LSV) paired with a rotating disk electrode (RDE) offers kinetic insight into the compounds' performance. The main kinetic parameters of interest for RFBs are the compound's diffusion coefficient and electron rate transfer constant.

The diffusion coeficient is very important for the performance of a redox flow battery and should be as high as possible to maintain high current densities at low states of charge and

reasonably low fluid flow rates [12]. If the diffusion coefficient is low, the current density will be restricted and lead to large overpotential, which appears as high/low voltage charging/discharging and poor attainable states of charge relative to theoretical [13], [14]. The RDE spins at constant, well-controlled rates to RDE ensure pure diffusion-limited redox behavior; the redox-active compound's diffusion coefficient can be calculated by Levich equation after collecting electrochemical data at different rotation rates:

$$I_L = (0.620)nFAD^{2/3}\omega^{1/2}v^{-1/6}C \quad (4)$$

where I_L is the limiting current (A), n is number of moles of electrons transferred in the half reaction, F is the Faraday constant (96485 C/mol), A is electrode area (cm^2), D is the diffusion coefficient (cm^2/s), ω is the angular rotation rate of the electrode (rad/s)v is the kinematic viscosity (cm^2/s), and C is the analyte concentration (mol/cm^3). The square root of the rotation rate is directly proportional to the limiting current and therefore a pot of I_L vs. $\omega^{1/2}$ (a Levich plot) is linear. The slope of Levich plot can be used to calculate the diffusion coefficient. Equation (1) can be rewritten as:

$$\text{Levich plot slope} = (0.620)nFAD^{2/3}v^{-1/6}C \quad (5)$$

The diffusion coefficient can then be used to determine the electron transfer rate constant, describing how fast the electron is transferred between the active compound in solution and the solid electrode. The electrochemical charge transfer rate constant (k^0) can be used to estimate the kinetics of RFBs, where low value would indicate sluggish power performance in RFBs, especially at lower current density and high states of charge where charge-transfer resistance dominates the overpotential [12] [13]. The rate constant can be calculated by the Nicholson's equation:

$$k^0 = \psi(\pi DnvF/RT)^{1/2} \quad (6)$$

where n, F, and D are defined in equation (1), ψ is kinetic parameter (ψ was obtained by using ΔE_p, where ΔE_p is the peak (E_{pc}) – the peak(E_{pa}) from cyclic voltammetry data) , and v is the scan rate (mV/s). From the D and k^0 values, the base characteristics of iron complexes can be investigated and compared to the literature and other RFB compounds. Since electrolyte additives will be studied to improve $Fe(bpy)_3SO_4$ solubility and stability, it will be necessary to establish the effect of additives on $Fe(bpy)_3SO_4$'s kinetic performance. The effect of solubilizing additives on $Fe(bpy)_3^{2+/3+}$ performance will be compared to the additive-free control data. If iron complexes with additives shows promise in these fundamental characteristics, they will be suitable in the construction and testing of a real redox flow battery. The battery performance, such as number of cycles, capacity, current density, and efficiency will then be determined and compared to literature and additive – free RFB performance.

1.5. RFB metrics and terminology

In order to investigate the battery performance, lab-scale flow cell tests will be constructed. Current density (mA/cm^2) has an important role in parameter, which define how much current is applying to the battery. The current (mA) that applies to the cell battery is calculated by:

$$\text{Current} = \text{Current density} * \text{Area } (cm^2) \quad (7)$$

The theoretical capacity of a battery's active compound is determined by its solubility (concentration), electrolyte tank volume, and – number of reversible electrons, calculated by Faraday's law.

$$q_{theoretical} = M*V*F. \quad (8)$$

where M is concentration, V is volume, and F is faraday constant (96485 CA/mol). The theoretical capacity of battery performance is calculated based on the limited active species. In this case, the

theoretical capacity is calculated with the concentration and volume of $Fe(bpy)_3SO_4$. Battery capacities are often reported mAh (or Ah l-l for RFBs), which can be calculated by:

$$\text{Battery capacity} = q * 3.6 \text{ (or } 3600) \tag{9}$$

In reality, 100% of theoretical capacity is never reached in operating RFBs. Thus, we define the percent utilization as:

$$\% \text{ util} = {}^{\text{achieved battery capacity}}/_{\text{theoretical battery capacity}} \tag{10}$$

Moreover, multiple efficiency of battery is calculated to compare the amount of energy that battery can deliver with other battery in realistic. Coulombic efficiency (CE), which helps to predict the lifespan of the battery [15]; Voltage efficiency (VE), which is an critical factor for battery performance and should be maximize; and Energy efficiency (EE), which represent the energy storage capability [16] are calculated by:

$$\text{CE} = \frac{\text{Discharge capacity}}{\text{Charge capacity}} * 100\% \tag{11}$$

$$\text{VE} = \frac{\text{Discharge voltage}}{\text{Charge voltage}} * 100\% \tag{12}$$

$$\text{EE} = \frac{\text{Energy density}_{discharge}}{\text{Energy density}_{charge}} * 100\% \tag{13}$$

For RFBs, the theoretical energy density incorporates the battery's output voltage and can be identified by the following equation:

$$\text{Energy density (Wh/L)} = nCFV/\mu_v \tag{14}$$

where n is the number of electrons involved in the cell reaction, C is the concentration of active materials, F is Faraday's constant of 26.8 Ah/mol, V is the cell voltage, and μ_v is the factor that represents the overall volumes of anolyte and catholyte []

The ideal RFB active compound would have multiple reversible electrons (high *n*), anolyte reduction and catholyte oxidation potentials near that of water (high V), and extremely high

aqueous solubility (high C). For example, doubling the active species aqueous solubility would instantly double the RFB's cost will also be important for commercialization and the targets are around $150/kWh.

The solubility will be investigated based on the relationship between concentration and light absorbance, given by the Beer-Lambert law:

$$A = \varepsilon bc \tag{15}$$

where A is the absorbance (unitless), ε is molar absorption coefficient that is constant for an analyte at specific wavelength, b is the path length of the cuvette and c is the concentration of the analyte.

1.6. Thesis purpose and objectives

The purpose of this research is improving $Fe(bpy)_3SO_4$ solubility in order to use as catholyte that is promising and reliable for RFBs. In addition, the degree and behavior of the dimerization process noted above is studied as a function of battery additives and operation. The compound will be tested with different additives such as ethylene glycol, nicotinic acid, butanol, etc. After determining the purity of the compound, the performance characteristics critical to RFBs such as redox behavior, solubility, or cycling stability will be tested.

The redox behavior of $Fe(bpy)_3SO_4$ with and without additives is studied with various electrochemical analytical technique. Relevant performance metrics are used to compare the capabilities of $Fe(bpy)_3SO_4$ catholyte solutions with different additives. Since high solubility is extremely important for RFBs, the solubility of the compound will also be tested with common additives, for example: isopropyl and sodium xylenesulfonate. Additives were chosen based on various compounds used in the literature which have different functional groups that may enhance

the solubility of the non-polar bipyridine-based ligand complex (hydrotropic effect) using amphiphilic molecules. The solubility will be tested at different concentration by Ultraviolet-visible (UV-vis) spectroscopy. After that, using the full RFB flow cell test, the charging/discharging cycle lifetime, efficiencies, capacity (utilization), and energy density can be determined. This information can be used to determine the battery performance as well as the degradation rate of the compound in percent per cycle or day.

If the compound satisfies the RFBs requirements, the performance of the compound will be considered for commercialization.

1.7. Literature review

Ruan et al. [9] reported high battery performance in a RFB using a $Fe(bpy)_3SO_4$ catholyte and Methyl Viologen anolyte that gave 99.8% of current efficiency over 200 cycles and can deliver around 90% of the theoretical capacity. One of the challenges noted is the solubility of $Fe(bpy)_3SO_4$; its aqueous solubility is about 0.8 M in pure water, but that drops to about 0.1 M in 1 M NaCl, a supporting salt (required) typically used in RFBs [9]. Typically, active compounds should have solubility >1M for RFB commercialization. Specifically, very few studies have investigated performance metrics at high concentrations of the active compound or additives to increase their solubility and long-term battery cycling stability such as butanol [11]. Moreover, they observed substantial voltage efficiency loss due to the decomposition of Fe (III) into the dimer and the resulting low voltage plateau during discharge.

Xie et al. [17] also introduced a battery that exhibits the capacity retention of 80% over 200 cycles using $Fe(bpy)_3Cl_2$ catholyte and $ZnCl_2$ anolyte. This battery has a open circuit of 1.82V, which is higher than Ruan paper (1.4V). The charging cut off of this paper was 2.2V but they never

reach 2.2V due to the transference of $Fe(bpy)_3^{3+}$ ions from the catholyte into the anolyte (membrane crossover) to react with Zn^{2+} ions when using Celgard 3501 membrane. The Nafion 115 membrane showed a better selectivity, which can avoid the leakage. A common issue of Zn in other batteries is the hydroxide or hydrogen ion crossover and react with Zn metal, which resulting in low CE and short lifetime. However, $ZnCl_2$/ $Fe(bpy)_3Cl_2$ flow battery did not have this problem. Thus, it can deliver more than 90% of CE and 86% of VE over 20 cycles.

On the other hand, Mun et al. [18] reported a non-aqueous RFB with 0.4M $Fe(bpy)_3(BF_4)_2$ catholyte and 0.2M $Ni(bpy)_3(BF_4)_2$ anolyte in $TEABF_4$ electrolyte. The cell voltage go up to 2.2V; and they achieved high CE and EE that is 904% and 91.8%, respectively. Nevertheless, there was an irreversible capacity of the system that explained by the ion crossover and polarization from the ion transport resistance of the membrane and the electrolyte.

In addition, Chen et al. [19] indicated that many pyridine - based of Fe (III) complexes are unstable because of nucleophilic attack by water. Thus, the stability of Fe (III) might be improved if the water activity is reduced. The Fe (III) complexes were tested with different additives in 0.5M H_2SO_4 solution by cyclic voltammetry and controlled potential electrolysis methods, and the result pointed out that a 1-butanol additive appeared to inhibit the Fe (III) decomposition process.

The dimerization process for $Fe(bpy)_3^{2+/3+}$ was deeply studied by Ehman (1969) [20]. The Fe (II) species (red) was oxidized to Fe (III) complexes (blue). The blue complex turned to brown oxo-bridged iron (III) complex during hydrolysis. This species can be reduced back to two Fe (II) complexes at low potential (equation 3), which is the voltage drop during discharge in Ruan et al.'s paper. According to Ehman, the dimerization process occurs between pH 2 and 6; moreover, this process is first order in any base that present H_2O, OH^- and bpy.

1.8. Summary

There are a lot of anolyte compounds have been explored for RFBs compared to possible catholytes. Organometallic complexes show particular promise and, among these active compounds, the tris(2,2'-bipyridine) complexes ($Fe(bpy)_3SO_4$) have a high redox potential, are easy to synthesize, and are built from inexpensive earth-abundant elements.

Solubility of the active compounds plays a major role in grid-scale electrical energy storage. Since the RFB operating principle is based on the ability of accepting and donating electrons, an active compound with high solubility will be able to provide more sources of electron acceptors and donors to the system. Consequently, an active compound with high solubility, will translate to an RFB with high energy density. Despite its many attractive qualities, the aqueous solubility of $Fe(bpy)_3^{2+/3+}$ is a current barrier to its commercialization.

CHAPTER II – METHODOLOGY

The iron bipyridine complex studied in this work is not commercially available so it must be synthesized first. Synthesis of this compound is quite simple from $FeSO_4$ and 2,2'-bipyridine: the organometallic complex quickly forms the deep red ferrous compound when these reagents are mixed in water or a binary solvent system.

2.1. Synthesis of iron complex

The iron complexes were synthesized following the procedures in literature [9] using iron (II) sulfate ($FeSO_4$) and excess bipyridine. A prepared aqueous solution of $FeSO_4$ was added slowly to an aqueous solution of excess bipyridine (mol ratio 3:1, respectively). The solution was stirred for 2 hours and resulted in a red solution. Excess free bipyridine was removed by washing with dichloromethane and all solvents were removed under vacuum. In order to confirm the identity of the compound, cyclic voltammetry (CV) and absorbance spectrometry (UV-Vis) were utilized.

2.2. Cyclic Voltammetry (CV)

As mentioned above, CV was performed to define the redox behavior of $Fe(bpy)_3SO_4$. In this experiment, a simple three electrode system that includes a reference electrode, counter electrode and working electrode, were used to run a CV (Figure 2.1). All electrochemical analysis in this work is performed using a Gamry Reference 600, PalmSens4, or CHI 760E potentiostat.

The reference electrode controls the potential of the working electrode. The potential difference between the reference and working electrodes is controlled by the potentiostat and allows scanning potentials over a wide range where redox processes might occur. For example, a

compound's redox behavior is typically initially screened between -1V to 1V at 100mV/s; the first potential scan (forward scan) will proceed from positive to negative potentials, from 1V to -1V over 20s, then the scan direction will be reversed from 1V to -1V (reverse scan) lasting 20s more. This is one cycle in which each scan is one segment and one cycle equivalent with 2 segments. For testing a compound, multiple cycles are often obtained to determine repeatability/reproducibility of the redox process(es). The potential range depends on the redox potential of tested compound, which should fall into supporting electrolyte windows (Chapter 1). There are several options available for aqueous reference electrodes, two of the most common being the saturated calomel electrode (SCE) and silver/silver chloride electrode (Ag/AgCl); Ag/AgCl is most commonly used in this research.

While the potential is applied between the reference and working electrode, the auxiliary/counter electrode allows current to pass, so that the reference potential can remain stable. An important role of counter electrode is preventing large current passing through the reference electrode, which causes its potential to change. The current and potential are measured by the potentiostat at the working electrode, where the reaction of interest takes place. The counter electrode is usually made of inert material such as platinum, gold, graphite, glassy carbon, etc. that does not degrade quickly and is sized larger than the working electrode.

The working electrode can be made of any conductive material and the most, common inert materials used are Au, Pt, and glassy carbon. The most common material to test for redox behavior in RFBs is glassy carbon (diameter = 3 mm), since the electrodes used for RFBs are typically carbon-based. The surface of the working electrode (electrode-electrolyte interface) is where the electrons transfer of the compound from solution to the external circuit take places.

To prepare for an experiment, each electrode was cleaned with different specific solution. The Ag/AgCl reference electrodes are stored in 3M KCl solution before use. The Pt counter electrode was cleaned with 0.5M H_2SO_4 and deionized water. Lastly, the surface of the glassy carbon working electrode was polished with 0.05μm polishing alumina on a wet diamond polishing pad. This process helps remove any impurities on the electrode surface and forms a mirror surface.

The setup of cyclic voltammetry for this study is shown in Figures 2.1 and 2.2, where the typical electrolyte is a solution containing 4mM $[Fe(bpy)_3]SO_4$ in 10mL of 1M NaCl. The CV was scanned at 50mV/s between 0.7 and 1V vs. Ag/AgCl, since that's where this compound can be oxidized from Fe(II) to Fe(III) forms.

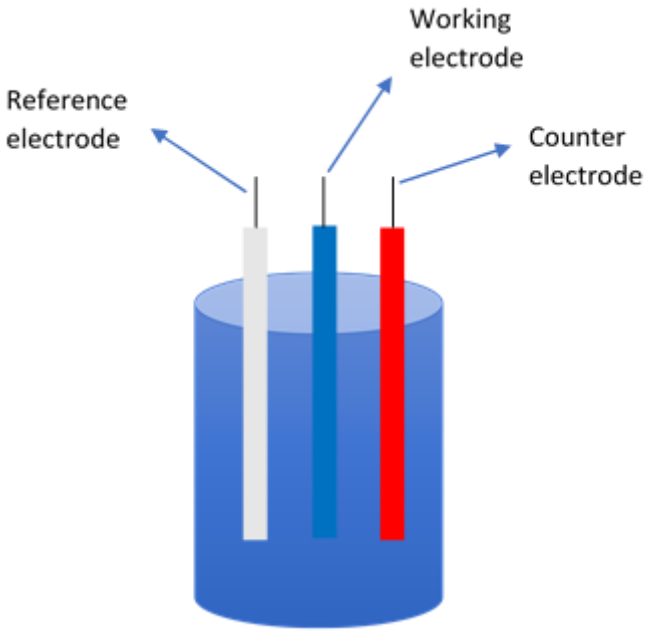

Figure 2.1 The three electrodes system for cyclic voltammetry.

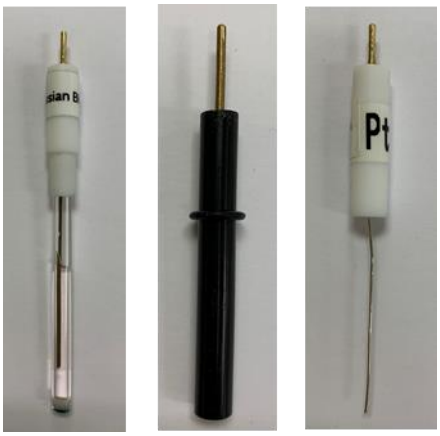

a b c

Figure 2.2 Three electrodes that use in CV. a. reference electrode b. working electrode c. counter electrode.

2.3. Linear Sweep Voltammetry

2.3.1. Rotating Disk Electrode

The Rotating Disk Electrode (RDE) use a hydrodynamic working electrode that is rotated at constant rates. The main advantages of the RDE is to (and vary) the diffusion layer of the working electrode, where reversible redox processes follow predictable behavior. Modulation of the rotation rate allows separation of the kinetic and mass transport-controlled components of a measured current [11]. Only the mass transports limited component of the current will respond to the modulation.

In RDE, the disk electrode is the working electrode, which is glassy carbon in this work. The electrode rotation rate (ω) is measured by rpm and is controlled by the instrument from 200-3000rpm. When the electrode rotates, the electrolyte solution is drawn up convectively towards the center of the disk electrode, where electrochemical reactions can occur, then

is flung outwards. Unlike CV, different patterns have chance to reach the working electrode while it rotating, which leads to flat line at the end of every scan of LSV.

To run an experiment with RDE, the setup is similar to three electrode system that is used for CV; it also includes three electrodes which are reference, auxiliary (or counter), and working electrode. In this research, the typical working electrode will be glassy carbon (4 mm for RDE), illustrated in Figure 2.3. The reference and counter electrodes (not rotated) are the same as CV.

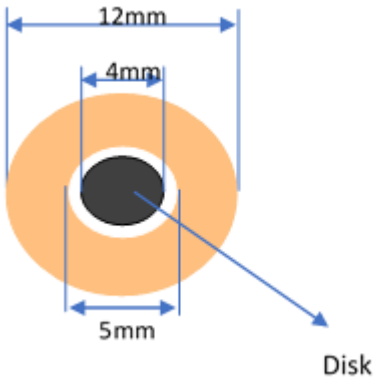

Figure 2.3. The diagram of rotating disk electrode.

2.3.2. Linear Sweep Voltammetry

Linear Sweep Voltammetry (LSV) is a technique corresponding to one segment from CV. Instead of multiple cycles, LSV only measures current of a segment but in different rotation rate. In theory, the limiting current is directly proportional with the electrode rotation rate. From RDE/LSV data, a Levich plot is constructed, where the limiting current is plotted against the square root of rotation rate, in order to calculate the active compound's diffusion coefficient and other important kinetic parameters. In this work, LSV was recorded for two solutions (additive and additive-free) from 300rpm to 3000rpm between 0.7V to 1.0V at scan rate 10mV/s. In a typical experiment, 4mM $Fe(bpy)_3SO_4$ is dissolved in 80mL 1M NaCl

solution with/without additives and LSVs are recorded over a series of different rotation rates for Levich analysis.

2.4. Bulk electrolysis

Bulk electrolysis (BE) is an electrochemical method in which the working electrode is held at a constant potential (potentiostastic) or constant current (galvanostatic) over time until the analyte solution is completely reduced or oxidized. This technique is most often used to determine the number of electrons transferred per molecule or, to electrosynthesize an absolute amount of analyte from a redox-active precursor. Unlike CV, BE has a large working and counter electrodes; also, the counter electrode is placed in a separate cell compartment to avoid the by-products. The working electrode of BE is Reticulated Vitreous Carbon (RVC). RVC has a special structure of open-pore foam structure resembling honey-comb that is composed solely of conductive vitreous (glassy/amorphous) carbon [21] (Figure 2.4). The large surface of the RVC not only allows it to react with large electrolyte volume/area, but also to work with variety of redox reactions or strong chemical because of its chemical robustness.

The aim of BE in this research is to oxidize the Fe (II) complexes completely in a potentiostatic process controlled by the potentiostat. A probe from UV-Vis is immersed into the bulk solution in order to measure the conversion of the red Fe (II) solution to blue Fe (III), followed by dimerization of Fe (III) to a brown dimer solution. The concentration of different species can monitor over the course of the reaction, depending on the concentrations and wavelengths studied. The dimerization rates can be investigated through the loss of Fe(III) complexes' visible absorption peak around 620 nm after determining its molar absorptivity from calibration curves. In order to prepare for the experiment, the working electrode and

counter electrode are rinsed with 1M H_2SO_4 and deionized water to remove all impurities. BE was performed using a Gamry Reference 600 potentiostat. The control solution was prepared by adding 0.025M of $Fe(bpy)_3SO_4$ into 1M NaCl. Multiple test solution was prepared by adding 1M additives to the control solution. The $Fe(bpy)_3SO_4$ solutions were fully oxidized by holding the working electrode at 1.2V and spectra were recorded during and after electrolysis.

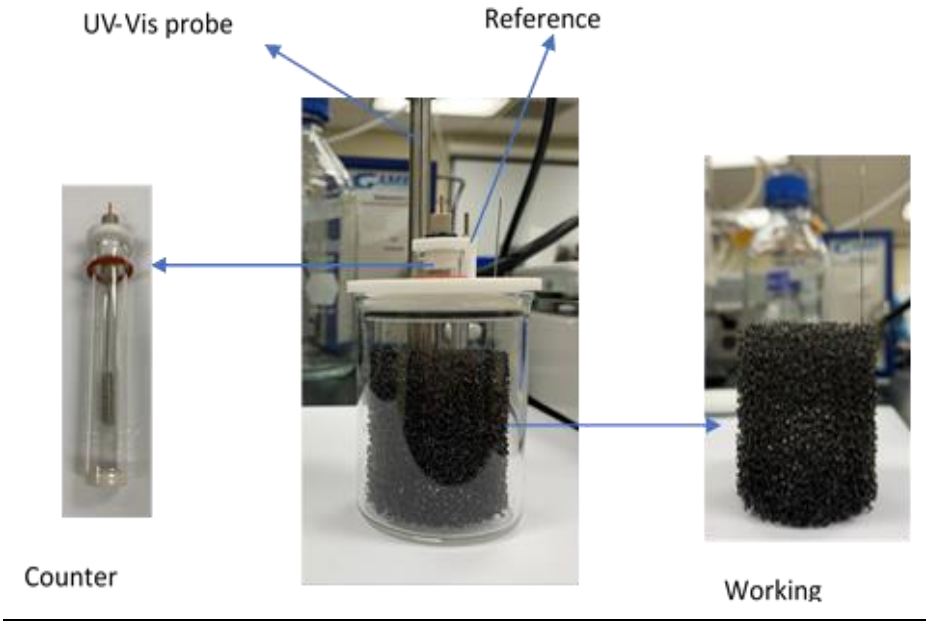

Figure 2.4. Bulk electrolysis set up.

2.5. Ultraviolet-visible absorption spectroscopy

Ultraviolet-visible spectroscopy (UV-Vis) was utilized to study the solubility of the iron complex. The main goal of UV-Vis is measuring the absorbance of the solution by passing a beam of light through the solution in cuvette at different wavelengths, which excites the electrons of the compound from ground state to excited state (Figure 2.5). The amount of light

absorption is proportional to path length and concentration (Beer-Lambert Law) and the wavelength region expresses the color of the solution. Only colored solutions will have absorbance in the visible region; otherwise, absorbance may occur in the ultraviolet and infrared regions. The wavelength of ultraviolet and visible are 100nm-400nm and 400nm-700nm, respectively. Beyond 700nm is the infrared region. In this work an ALS SEC2022 array spectrometer is used, which captures absorbance over the entire wavelength range (from 200-1000 nm) instantaneously.

In a typical experiment, control solutions were prepared by adding 0.1M, 0.15M, 0.2M ,0.25M and 0.3M of $Fe(bpy)_3SO_4$ into 1mL of 1M NaCl solution. Since UV – Vis cannot detect the sample at high concentration, the supernatant of each sample must be diluted by 1500 times (~0.5mM). The spectra of each sample were collected and analyzed at wavelength 298nm, the most prominent absorbance peak. The same procedure was applied to solutions with additives. Solubility limits are identified by absorbance peak at wavelength 298nm. As mention above, increasing the concentration of $Fe(bpy)_3SO_4$ means increasing the absorbance peak. If the absorbance peak keeps increasing, we assume that $Fe(bpy)_3SO_4$ has not reach the maximum solubility yet. If two to three concentrations give the same peak of absorbance, we assume that the solution is saturated and the solubility of $Fe(bpy)_3SO_4$ is max.

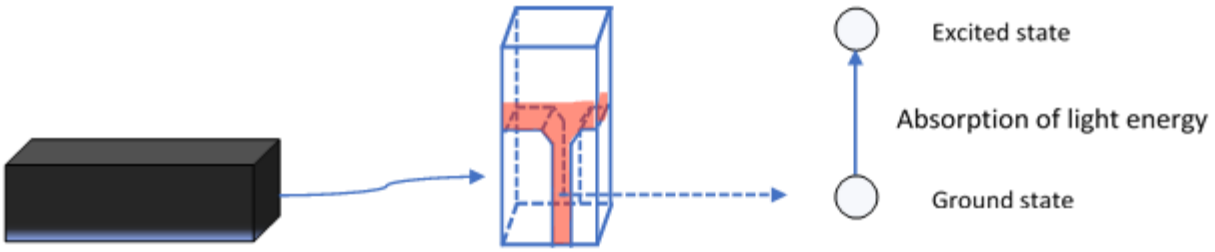

Figure 2.5. Diagram of UV-Vis absorption data collection.

2.6. Battery performance

The overall set up for testing redox flow batteries is shown in Figure 2.6. Basically, every battery test includes battery cell, battery cycler (Landt), catholyte, anolyte and pump. Figure 2.8 represents the lab scale battery to study the performance of iron-complexes. The catholyte and anolyte are pumped directly into the battery cell for electron transfer during charging/discharging; these solutions are constantly recirculated between the reservoir bottles and the battery stack. The flow rate of catholyte and anolyte was controlled by a 2-channelperistaltic pump (Golander). The system was placed inside the glove box filled with nitrogen to prevent the attack of oxygen on the charged anolyte. Electrical connections are made to the battery cycling system, which was placed outside of the glove box.

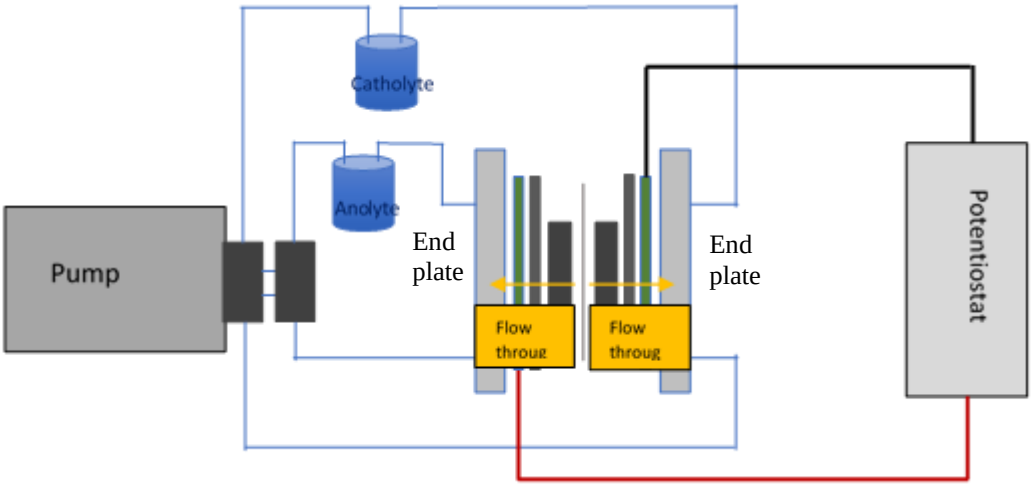

Figure 2.6. Diagram of battery performance.

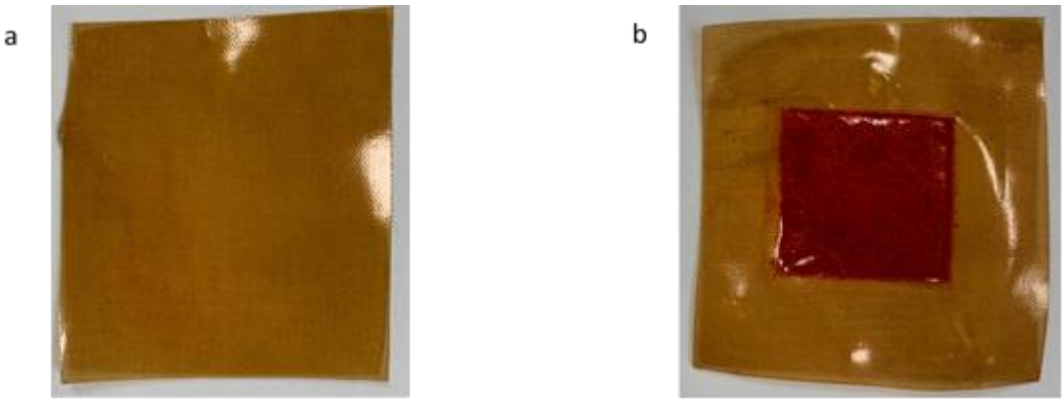

Figure 2.7. CSO membrane a. before b. after the battery performance.

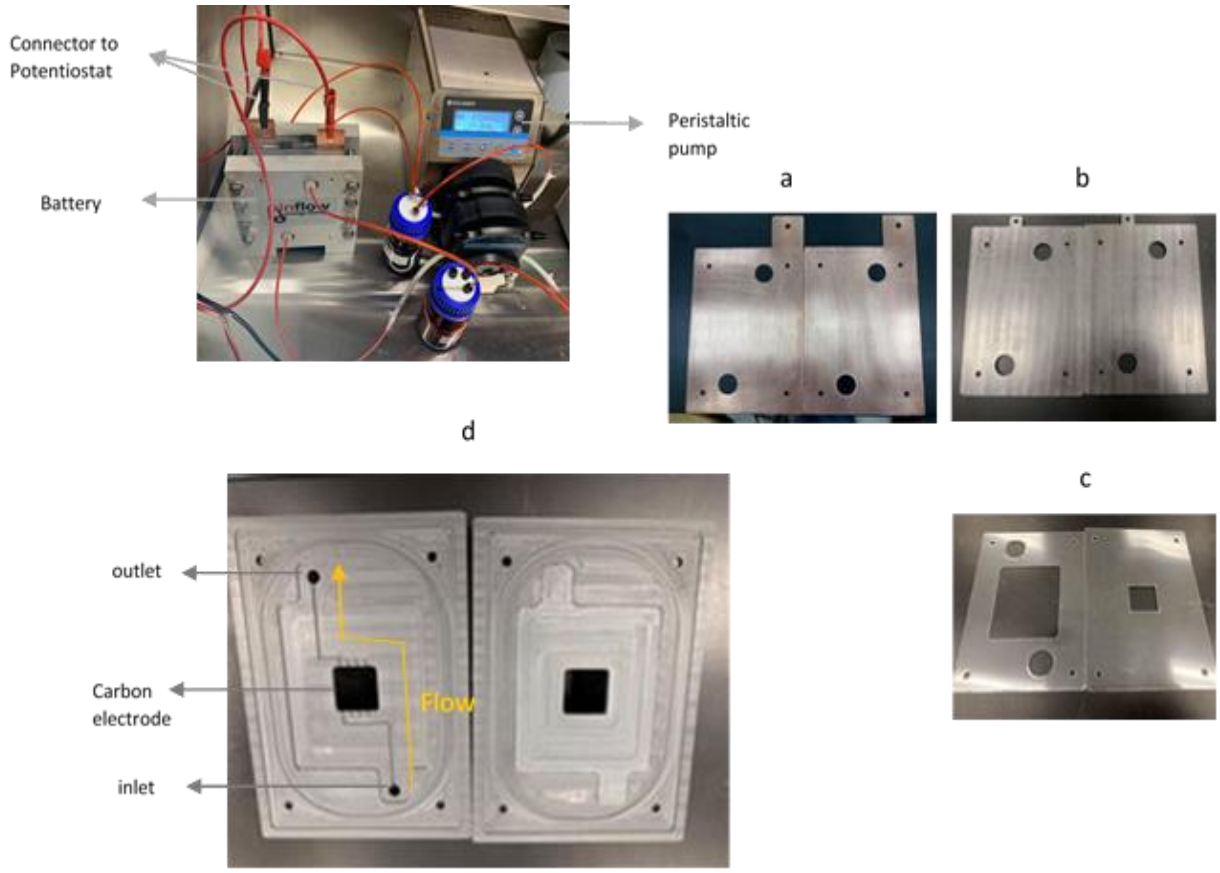

Figure 2.8. Lab scale battery performance. a. Copper current collector b. carbon-polymer composite plates c. carbon-polymer composite plate d. flow frames.

2.6.1. Battery cell

The battery cell stack was obtained from Pin FlowES. It consists of 2 aluminum end plates, 2 copper current collectors, 4 carbon-polymer composite plates, 2 flow frames, 2 carbon felt electrodes (4.6 mm thickness) and a membrane (Figure 2.8). The geometric active area of the cell is 5cm^2.

Carbon felt electrodes have an important role in RFBs performance. In order to activate the carbon felt electrode, it was treated in a furnace at 450C for 4 hours then stored under vacuum.

This process help introduces hydrophilic functional groups on the surface of electrode [23] to gain a better response to catholyte and anolyte solutions. The treated electrodes were immersed in 1M KCl before assembling the battery in order to improve performance. All the battery components and the stack were uniformly tightened to 8N-m in order to compress the carbon felt electrode for higher performance from the battery [24] and prevent leakage of solutions.

As mentioned in Chapter 1, the membrane is a barrier that prevent cross mixing of catholyte and anolyte solutions. In this study, we use a cation exchange membrane (Selemion – CSO that pre – soaked in 1M KCl solution overnight to obtain a selective permeability for cations (K^+ or Na^+ from the battery's supporting electrolyte). Figure 2.7 showed the CSO membrane before and after battery performance. After performance, the membrane got stained. It was the membrane cross problem for most of the battery.

The basic structure of the battery cell is shown in Figure 2.8. The catholyte and anolyte are pumped into the cell from the bottom to the top to prevent channeling within the electrode. There was one inlet and outlet for each flow frame. The compressed carbon felt electrodes, are in the middle of the flow frames and contact directly with CSO membrane.

2.6.2. Electrolyte

In the battery tests, as with other experiment, a control battery will serve as the baseline data to compare with RFBs containing additives. In a typical battery, the catholyte is prepared by dissolving 0.1M $Fe(bpy)_3SO_4$ into 20mL of 1M KCl solution, while the anolyte was prepared by dissolving 0.15M AQDS into 30mL of 1M KCl solution. The different in volume and concentration is required to assure catholyte is the limited side. There is a different pH between catholyte (pH = 3.6) and anolyte (pH = 10.3) solutions. Therefore, a specific amount of HCl that

added into anolyte solution to adjust the pH. The peristaltic pump was used to control the flow rate, which was set up at 26.4rpm (calibrated to deliver ~20mL/min). As mentioned above, the anolyte is very sensitive to oxygen; therefore, all battery test were set up and performed in the glove box (O_2 < 200rpm).

2.6.3. Battery performance

There are several tests of battery cycling to be performed. The basic charge – discharge cycling was set up galvanostatically at a current density of 20mA/cm^2, (100 mA for the 5 cm^2 PinflowES cell), which is typical in the literature. The battery was charged up to 1.5V and discharged to 0.1V, controlled by a battery cycler (Land Instruments). Each battery is typically cycled for 30-50 cycles with voltage data recorded every 5 seconds. The voltage is plotted vs capacity to analyze voltage efficiency, energy efficiency, power density, capacity fade, and the $Fe(bpy)_3SO_4$ dimerization process. Long-duration cycling, over 200 cycles, would be tested later with highest concentration of $Fe(bpy)_3SO_4$, to determine cycle and calendar time decay rates, hugely important metrics for long-life RFBs. For the power density tests, the battery was fully charged at 20 mA/cm^2; then discharged at different current densities from 10mA/cm^2 to 130mA/cm^2 and the voltage was recorded.

To evaluate the dimerization process, rest steps of varying durations were set between the charge – discharge steps. The parameter set up is shown in Figure 2.9. The battery was set to cycle normally for 3 cycles; then, after fully charging at cycle 4, the battery rests for 15 mins before entering the discharge state. This process was repeated for 30 mins, 45 mins and 60 mins rest times.

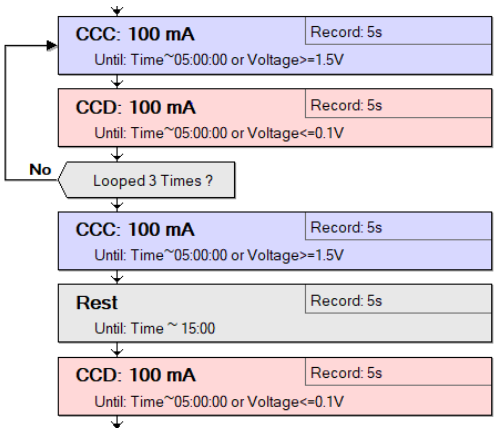

Figure 2.9 The sequence and parameters of rest mode test for dimerization studies. CCC: constant current charge, CDC: constant current discharge.

CHAPTER III – RESULTS AND DISCUSSION

To investigate the effect of additive on solubility and dimerization, the control was analyzed first, which include all the kinetic studies and battery performance; then used as the baseline to compare with the additive's solutions.

3.1. Characterization of Iron-complex

3.1.1 Cyclic Voltammetry

CV was carried out to confirm the electrochemical behavior. Figure 3.1 presents the cyclic voltammogram of $Fe(bpy)_3SO_4$ demonstrating Fe (II)/Fe(III) redox reaction. The result shows a reversible reaction on glassy carbon electrode, which meet the requirement of active compound for RFBs. The separation between cathodic and anodic peak is ~65mV, which tell us that the compound is an electrochemically reversible one electron redox couple. The center is around 0.85V vs Ag/AgCl (~1.04V vs SHE) that match with reported paper [9]. There is no shift or change after few cycles, which suggesting the stability of $Fe(bpy)_3SO_4$ in the test solution 1M NaCl which a common RFB supporting electrolyte [9].

The CV of $Fe(bpy)_3SO_4$ is used as the baseline to compare with other solution that include additives used for solubilization and/or dimer inhibition. CVs of $Fe(bpy)_3SO_4$ with suitable additives should maintain electrochemical reversibility. The CV is also extended in figure 3.2. The second reductive peak of $Fe(bpy)_3SO_4$ is represent for the dimer, which is irreversible. This is because the dimer is able to convert back to $Fe(bpy)_3^{2+}$, but the $Fe(bpy)_3^{2+}$ is oxidized to $Fe(bpy)_3^{3+}$ and not dimer.

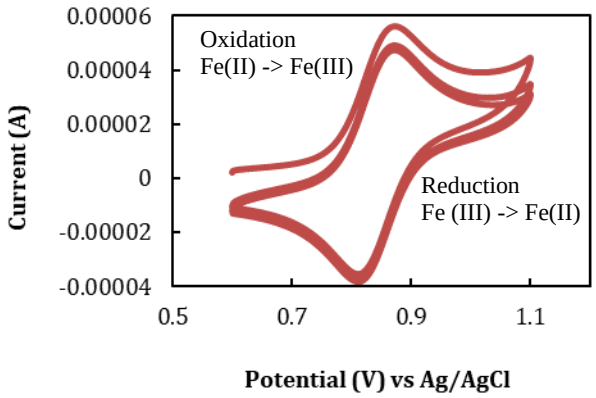

Figure 3.1 The cyclic voltammogram of 4 mM $Fe(bpy)_3SO_4$ in 1M NaCl at 50mV/s on a glassy carbon working electrode.

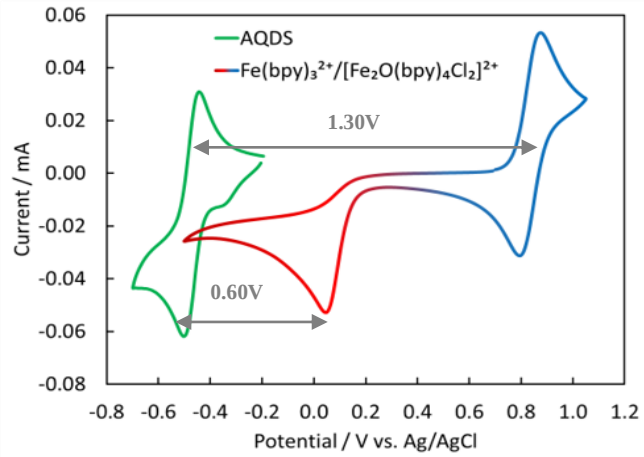

Figure 3.2 Cyclic voltammetry of a $Fe(bpy)_3SO_4$/dimer solution (blue/red) and AQDS (green).

In order to investigate the performance of the iron-complex as an RFB catholyte, Anthraquinone-2,7-Disulfonic acid Disodium salt (AQDS) was chosen as the anolyte and the most common supporting electrolyte was 1 M KCl. There are four main benefits to using AQDS as the anolyte. First, AQDS has low redox potential (~ -0.5V vs Ag/AgCl) (Fig 3.2). Thus, the open circuit of this redox couple can go up to 1.3V, which approaches that of vanadium redox flow batteries (1.1V – 1.5V). The open circuit between dimer and AQDS is

0.6V. Second, AQDS has well demonstrated performance for batteries at near-neutral pH [25] that meet the requirement of this research, since our iron complex is only stable over the range from pH 3-9. Third, AQDS can exchange up to two electrons per molecule (Fig 3.3) [26]. And lastly, anthraquinone derived from nature, which is all-organic/earth abundant elements. These benefits of AQDS, which will be used in excess, helps us to focus and study the catholyte. Figure 3.2 also shows the open circuit between the dimer and the AQDS, which is 0.60 V vs Ag/Ag/Cl.

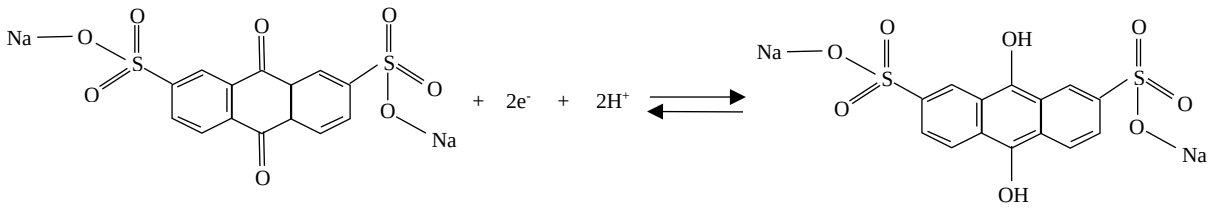

Figure 3.3 Redox reaction of Anthraquinone-2,7-Disulfonic acid Disodium salt

To confirm about the represent of Iron – complex in the solution, UV-Vis spectra will also be analyzed later.

3.1.2 Kinetic studies

To further understand the electrochemical kinetics of $Fe(bpy)_3SO_4$, RDE and LSV was used to investigate electron transfer rate and diffusion coefficient. LSVs were recorded at different rotation rate ranging from 300rpm to 3000rpm, shown in Figure 3.4a. The flat line indicates the limiting oxidation current, I_L, which can be used to construct Koutecky-Levich plots (Fig3.4b). As mentioned in Chapter 2, different particles have chance to reach the electrode; thus, the faster of the rotation rate, the more particles reach which lead to higher limiting current. The limiting current of each rotation rate was plotted versus square root of rotation rate and shows a linear relationship.

The slope of the Koutecky - Levich plot will then be used to determine diffusion coefficient and eventually electron transfer rate constant by equations (5) and (6), which were discussed in chapter 1. The diffusion coefficient of $Fe(bpy)_3SO_4$ in 1M NaCl was calculated to be 2.08 x 10^{-6} $cm^2.s^{-1}$ and the transfer rate is 3.2 x10^{-2} $cm.s^{-1}$. These values are comparable to other active compounds of RFBs. It shows that the current density will not be restricted, and the compound has a good attainable state of charge relative to the theoretical [13].

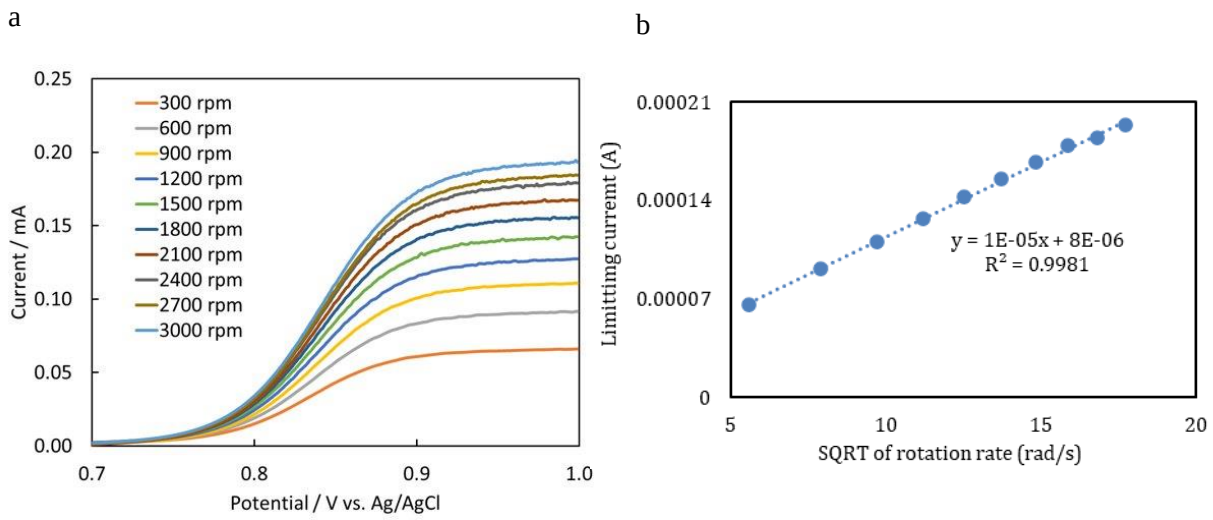

Figure 3.4 The kinetic study of 4mM $Fe(bpy)_3SO_4$ in 1M NaCl. a. linear sweep voltammogram at scan rate 10mV/s b. Koutecky-Levich plot.

3.1.3 Battery performance

A lab scale of RFB was constructed with $Fe(bpy)_3SO_4$ and AQDS as catholyte and anolyte, respectively. The solutions were prepared by adding 0.1 M $Fe(bpy)_3SO_4$ to 1M KCl for catholyte and 0.15 M AQDS in 1 M KCl for anolyte. We used KCl as supporting electrolyte because AQDS has good performance in KCl [25], [26]. AQDS is a two-electron carrier and thus the anolyte capacity is in far excess, so the battery performance is completely limited by the catholyte. The

data from this battery will serve as the control data for later studies into additives; and the results are showed in Figure 3.5.

Figure 3.5 (a) represents the charge – discharge voltage – capacity data of representative cycle 15, 30 and 50. The open circuit of the battery is very high for aqueous battery, around 1.25V in agreement with the CV of $Fe(bpy)_3SO_4$ and AQDS. During charge, the catholyte can deliver 130C (39.6mAh), which is 67% of the theoretical capacity based on the volume and concentration of the electrolyte (equation 8). This value is typical for redox flow batteries, since mass transport to the electrode limits capacity utilization at low concentrations of electrolyte as the battery nears full discharge (0% SOC). In general, the catholyte delivers a stable capacity during many cycles (Fig. 3.5b), which makes $Fe(bpy)_3SO_4$ promising for long-term energy storage. As mentioned in Chapter 1, Fe (II) is oxidized to Fe (II) during charge, then there are two reactions that can occur during discharge (equations 1 and 3). The monomer (Fe(III)) is converted back to Fe (II) at ~1.03 V (vs SHE) and the dimer is converted back to Fe(II) at ~0.35 V (vs SHE). The two plateaus during the discharge in Fig. 3.5a confirm the presence of both monomer and dimer that formed during charge. The voltage drop between monomer and dimer discharge is about 0.6V leading to low voltage and energy efficiencies (~65% for both, Fig. 3.5b). The voltage and energy efficiency have an important role that reflect the cell overpotential at high current densities [27]. The trend of voltage efficiency, coulombic efficiency and capacity utilization were outlined in Figure3.5 (b). Nevertheless, the coulombic efficiency average stayed around 99.7%, which suggested that all the monomer and dimer species were able to completely convert back to Fe(II) by the end of the discharge phase. The result of power density was recorded in Figure 3.5 (c) by discharging at various currents within the monomer plateau. The peak power density output of this battery is $90mW/cm^2$ at $120mA/cm^2$, which will be compared to batteries containing additives.

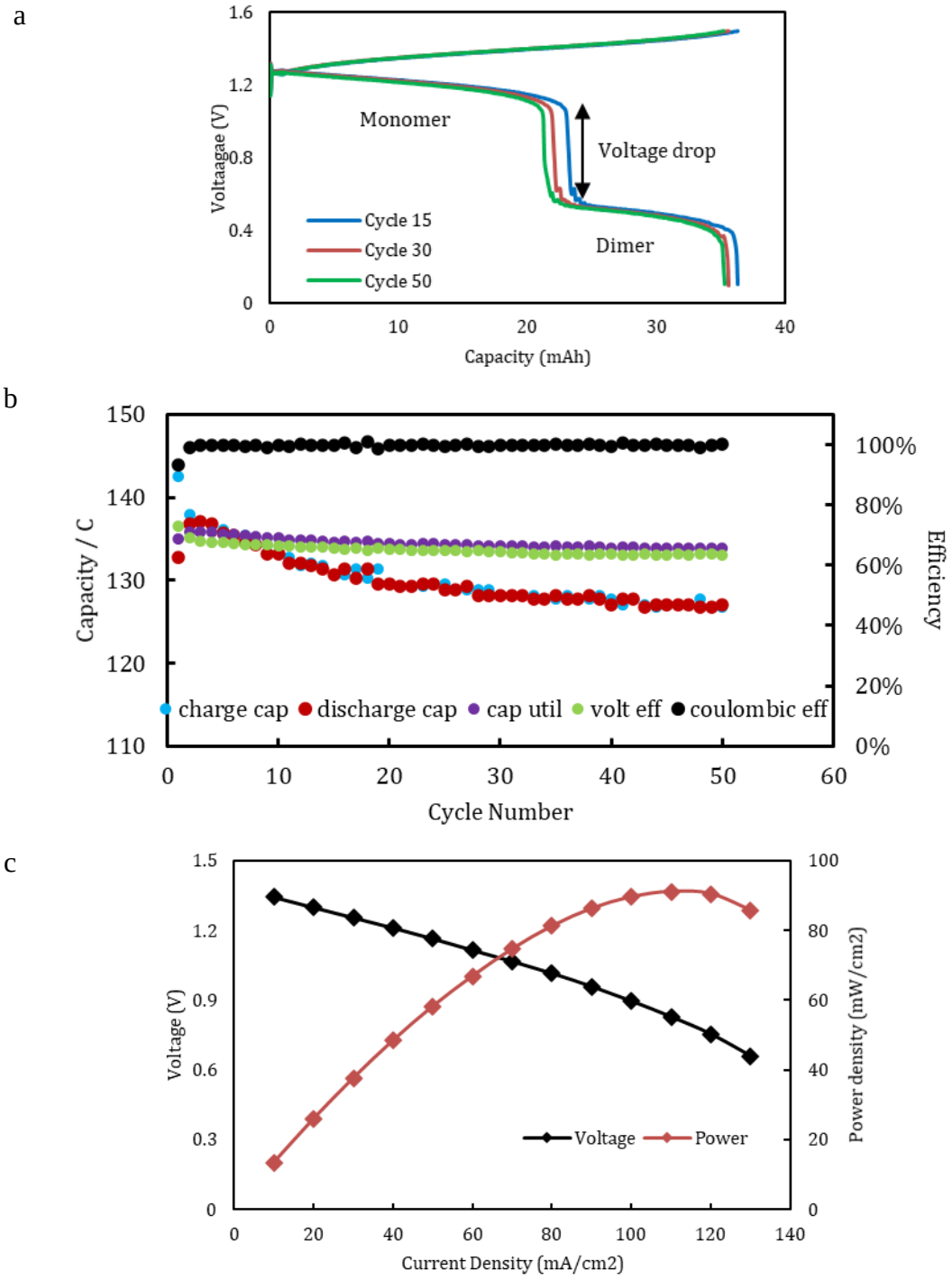

Figure 3.5 Battery performance of 0.1M $Fe(bpy)_3SO_4$ and 0.15M AQDS in 1M KCl. (a)Charge – discharge at different cycle number at current density of 20mA/cm^2, flow rate 20mL/min. (b)

Cycling performance with efficiency and capacity. (c) Cell voltage and power density (polarization) curves.

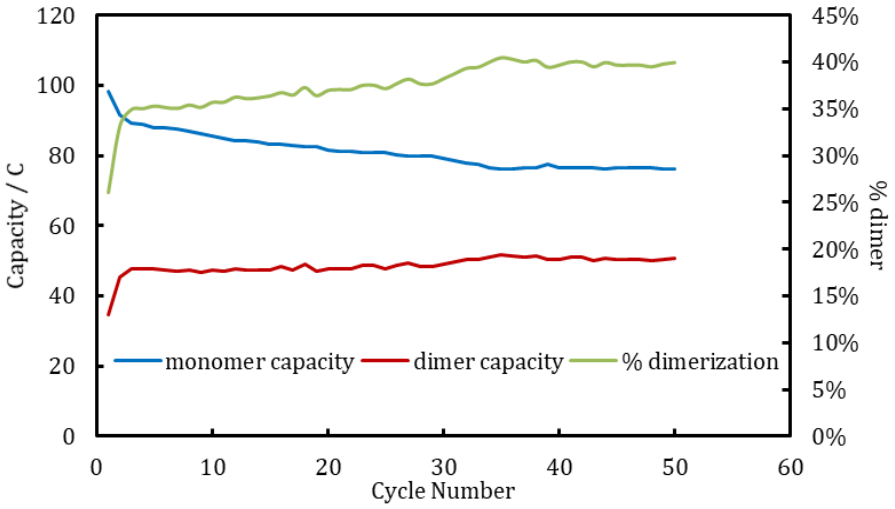

Figure 3.6 The analysis of dimerization process during 50 cycles.

The dimerization process was further studied by specifically analyzing the monomer and dimer capacities (Figure 3.6), i.e the length of each plateau from Fig 3.5a over 50 cycles. At the beginning of the cycling, the monomer capacity was high and occupied around 75% of the discharge capacity. During cycling, the monomer capacity decreased somewhat, and the dimer capacity was increased accordingly. At the end of the charging cycle 50th, the monomer capacity is 60% of the discharge capacity. This relationship was expressed through the percentage of dimerization, which increased from 25% to 40%. The dimerization process was studied deeper with the additives, which will be shown later.

3.2. Increasing $Fe(bpy)_3SO_4$ Solubility

The Figure 3.7 illustrate the spectra that collected from only the ligand, bpy in Acetonitrile and the organometallic complex $Fe(bpy)_3SO_4$ in 1M NaCl. The bpy solution is colorless, so its

absorbance was only expressed under ultraviolet region. Upon complexation, $Fe(bpy)_3^{2+}$ exhibits a red color, so it absorbs in the violet visible region, specially it has characteristic metal to ligand charge transfer band at 527 nm. The main different between these two spectra is the region from 430nm to 570nm, which represent for $Fe(bpy)_3^{2+}$. These spectra confirm that the iron – complex was synthesized successfully. For solubility studies, the absorbance of each concentration is collected at wavelength 298nm due to a clear and sharp peak.

To see the effect of different additives, the solubility of $Fe(bpy)_3SO_4$ in Water and 1M NaCl was first collected as the baseline data. A $Fe(bpy)_3SO_4$ sample was prepared to different concentration from ~0.1 M to 0.3 M. The sample was stirred for 20mins and ultrasonicated to maximize the dissolution of $Fe(bpy)_3SO_4$. The centrifuge was used to separate the saturated (supernatant) and $Fe(bpy)_3SO_4$ that do not dissolve (pellet) (Fig 3.9). Due to strong light absorption at these high concentrations, the supernatant of each sample was be diluted by 1500 times before measuring absorbance. By this method, we expect absorbance to increase up to the solubility limit of the compound, then level off.

Thanks to the Beer-Lambert Law (equation 15), the absorbance of peaks in the spectra are directly proportional to concentration; therefore, higher concentration give higher absorbance. The maximum concentration is reached, when the increase of absorbance with concentration becomes flat. As a result, the highest concentration of $Fe(bpy)_3SO_4$ in 1M NaCl is ~0.15M (Fig. 3.8) which agrees with the literature [9]. From the baseline, we calculate the molar absorptivity of $Fe(bpy)_3SO_4$ (ε = 31,853) @298nm by using equation 15.

There are a lot of additives could be added into the solution to test for the solubility. Rational selections of additives were made based on compounds with representative functional groups and/or amphiphilic properties that might help increase the solubility of Febpy.

Hydrotropic agents such as Urea, Ethylene glycol (EG), Sodium Xylene sulfonate, have been shown to successfully increase the solubility of RFB active compounds before (Urea for azobenzene [28], EG for AQDS [25]). However, instead of preparing various concentrations from 0.1 M to 0.3 M, the sample with additives was prepared at 0.15 M $Fe(bpy)_3SO_4$ in 1 M NaCl and added 1 M additives to set standard concentrations for reproducibility studies. If all the $Fe(bpy)_3SO_4$ dissolved at 0.15 M, then more $Fe(bpy)_3SO_4$ was added until the maximum concentration is reached. Then the same process of dilution and spectrum collection was repeated with the supernatant. The absorbance of the saturated solution was also collected at 298nm. Using the molar absorptivity that was calculated previously, we plug the absorbance of saturated solution in Beer-Lambert equation to calculate for the maximum solubility of $Fe(bpy)_3SO_4$. Figure 3.10 shows the maximum solubility of $Fe(bpy)_3SO_4$ in different solvents (DMSO, IPA), supporting salts (NaCl, NaNO3, NaF), and additives (NaXS, …) which could be used in RFBs.

The electrolyte of aqueous RFBs (or any electrochemical cell) requires a supporting salt to balance charge between the catholyte and anolyte. The ions of this supporting electrolyte move freely through the membrane (the salt bridge) to balance charge within the cell during operation. Therefore, although the solubility of $Fe(bpy)_3SO_4$ in water is relatively high at ~0.6 M, we cannot use only water with $Fe(bpy)_3SO_4$ to run the RFBs. 1 M NaCl and $NaNO_3$ reduce catholyte solubility to similar concentrations of $Fe(bpy)_3SO_4$, around 0.15 M. NaF gave good solubility of $Fe(bpy)_3SO_4$, but battery tests using this salt were unsuccessful, perhaps due to incompatibility of battery materials with the fluoride ion. While DMSO apparently offers improved solubility, mixed solvents (~50%) might require other modifications in RFB materials to perform well; thus the mixture solvent of DMSO and water are

not an area that we will focus on at this time. As the results show, the range of promising additives and alternative salts was narrowed down to IPA and $C_6H_4N_2$ (4-pyridine carbonitrile), which gives 0.35 M, 0.36 M $Fe(bpy)_3SO_4$, respectively. The remainder of this research will focus on fully characterizing IPA as a low-cost, solubility enhancing additive for the $Fe(bpy)_3SO_4$ catholyte. The solubility of $Fe(bpy)_3SO_4$ increases to ~0.35M by adding 1 M isopropyl alcohol (IPA) into the solution. As mentioned above increasing the solubility means increasing capacity and energy density; so, IPA will be used for further tests on battery performance. We will demonstrate its capabilities by performing battery cycling, studying its effect on dimerization and long-term cycling stability compared to the control data of the catholyte in supporting electrolyte without additives.

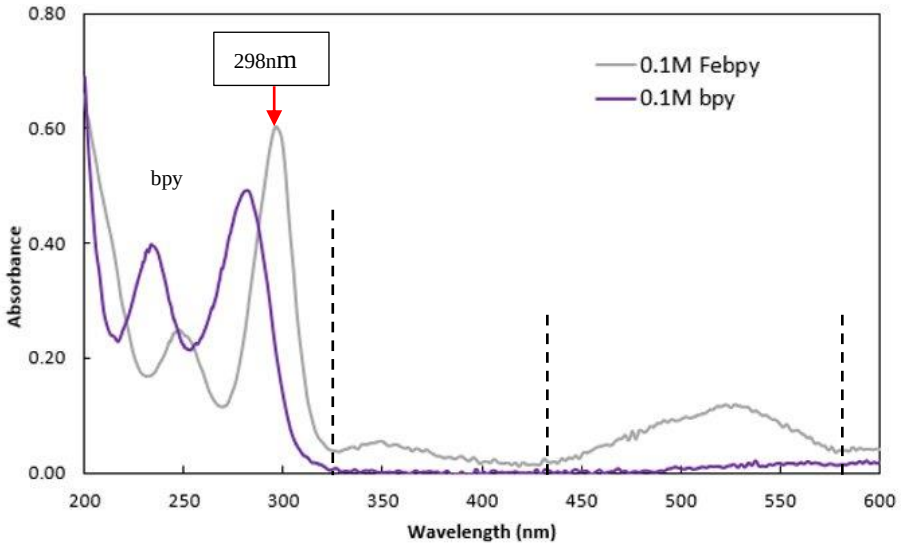

Figure 3.7 The UV-vis absorption spectra of 0.25 mM $Fe(bpy)_3SO_4$ and bpy.

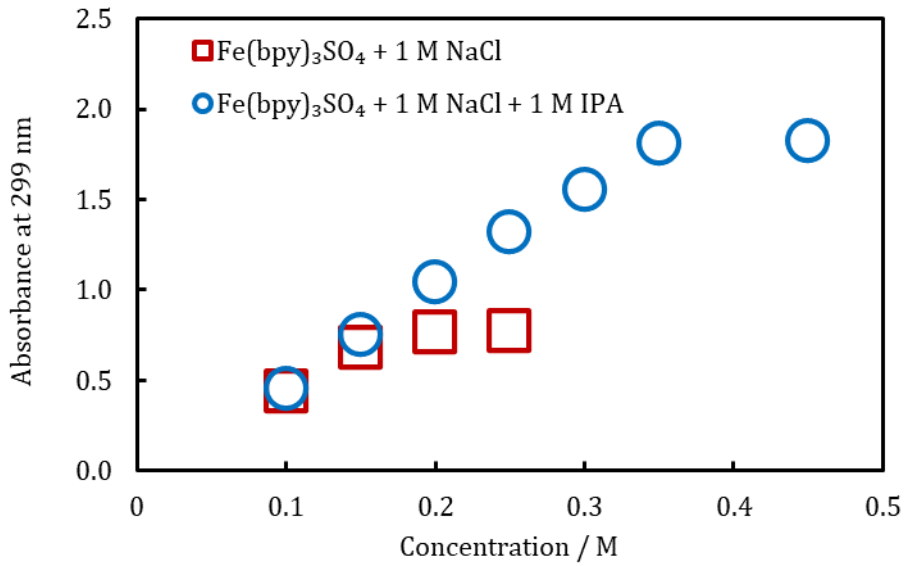

Figure 3.8 The solubility test of $Fe(bpy)_3SO_4$ with and without additives express through the relationship of absorbance and concentration.

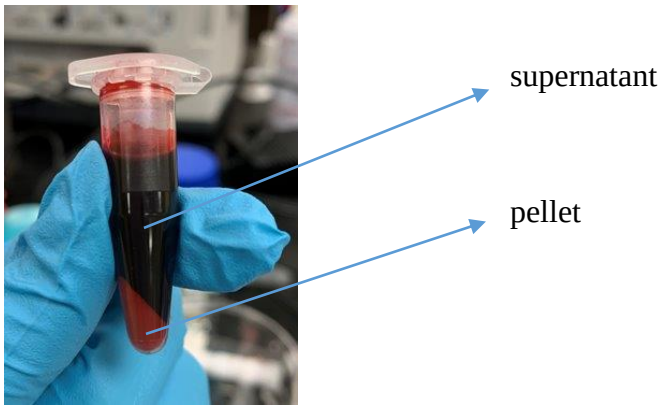

Figure 3.9 Saturated solution of $Fe(bpy)_3SO_4$ in water after centrifuge.

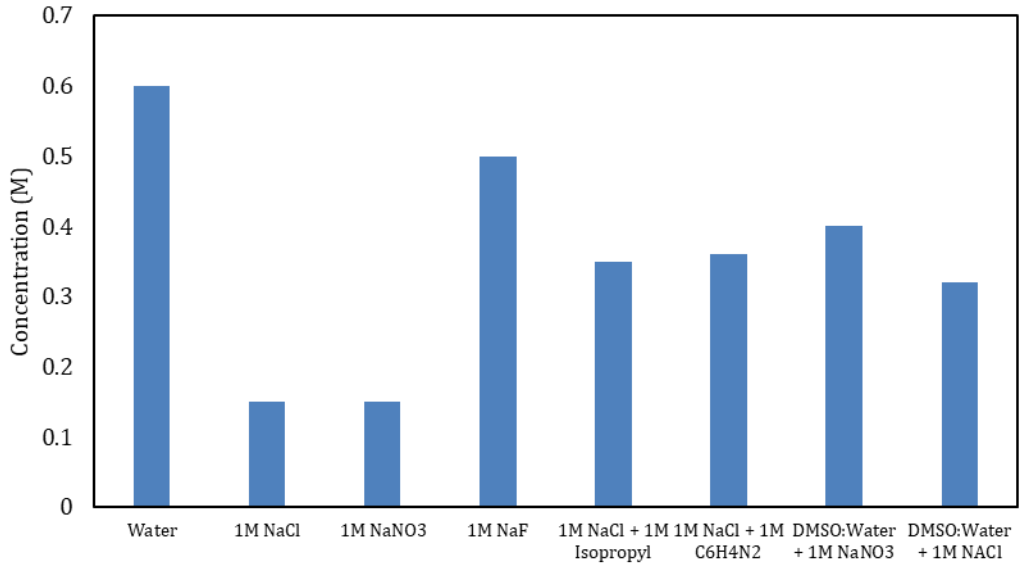

Figure 3.10 A summary of maximum solubility of $Fe(bpy)_3SO_4$ in different solvent and additives.

3.3. Study of dimerization

The second major goal of this research is to discover an additive that could inhibit dimerization of the Fe (III) complex, which degrades battery performance as discussed for the control battery above. In this study we will explore the influence of additives on the rate of dimerization of the Fe (III) species.

3.3.1 Bulk electrolysis of low concentration catholyte

In order to specifically study the dimerization process without constructing whole batteries, Bulk electrolysis (BE) with in situ UV-Vis probe was used to investigate the dimerization rate of $Fe(bpy)_3SO_4$ in different solvents and additives. By this method, $Fe(bpy)_3^{3+}$ is electro-generated by oxidizing a solution of $Fe(bpy)_3^{2+}$, while an *in situ* UV-vis probe measures changes in

absorbance over time that correspond to the conversion of $Fe(bpy)_3^{3+}$ to the Fe2O(bpy)4Cl2… dimer (equation 2).

To evaluate how the concentration of $Fe(bpy)_3^{2+}$ will change during electrolysis. We cannot analyze the $Fe(bpy)_3^{2+}$ solution at high concentration because of the noise that came from UV-Vis spectra when detected the sample at high concentration. Therefore, a low concentration was prepared to also study the changes of $Fe(bpy)_3^{2+}$. The solution was prepared as 0.25 mM $Fe(bpy)_3SO_4$ in 1 M NaCl solution. The solution was fully oxidized by BE at 1.2V; after that it was fully reduced at 0.2 V to investigate the difference between $Fe(bpy)_3^{2+}$, $Fe(bpy)_3^{3+}$ and $[Fe_2O(bpy)_4Cl_2]^{3+}$ species. UV-vis spectra were collected during and after electrolysis for low concentration solution.

Figure 3.11a illustrates the evolution of UV--vis spectra during and after electrolysis of the low-concentration $Fe(bpy)_3^{2+}$ solution. The absorbance around 240nm and 330nm increases, while the peaks around 300nm, 350nm and 500nm decrease. We can see this trend is totally opposite during reduction, when the Fe(III) solution (after having time for complete dimerization) is reduced back to $Fe(bpy)_3^{2+}$, as shown in Figure 3.11b. The absorbance peak around 530 nm is the characteristic MLCT peak of $Fe(bpy)_3^{2+}$, discussed above. It decreases until A=0 during oxidation, which means all the $Fe(bpy)_3^{2+}$ species in the solution is oxidized to $Fe(bpy)_3^{3+}$ and vice versa for the reduction spectra. The spectra are nearly identical before oxidation and after reduction; however, they located at similar wavelengths and are qualitatively very similar, as expected indicating complete recovery of $Fe(bpy)_3^{2+}$ after dimerization and reduction. This study allows us to isolate and distinguish the spectra between $Fe(bpy)_3^{2+}$, $Fe(bpy)_3^{3+}$ and $[Fe_2O(bpy)_4Cl_2]^{3+}$ in Figure 3.11c. There is a clearly different of $Fe(bpy)_3^{2+}$ peak at 500nm, which in agree with UV-vis during electrolysis of oxidation

and reduction. While we were hoping to see clear differences between the three spectra so that each could be reliably identified through UV-vis (especially the dimer), however the dimer spectrum is virtually indistinguishable from Fe (III) monomer features. This is the reason why we will use high concentration and analyze the $Fe(bpy)_3^{3+}$ peak at 610nm later. At high concentrations the LMCT band of $Fe(bpy)_3^{3+}$ can be seen as shown above in Fig. 3.12, however absorbance is too strong at the shorter wavelengths to confidently identify the presence of the dimer.

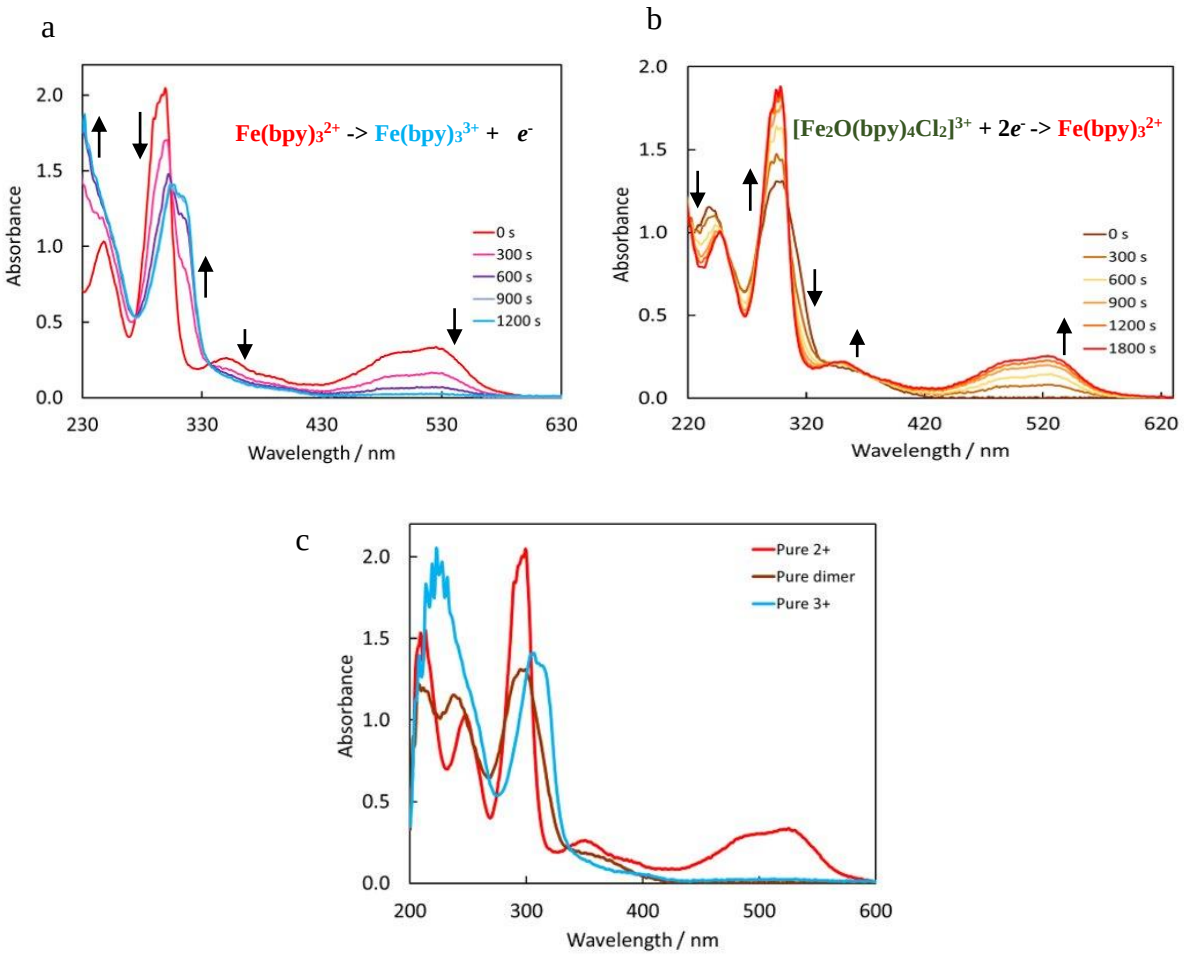

Figure 3.11 UV-Vis absorption spectra during electrolysis of 0.25 mM a. $Fe(bpy)_3^{2+}$ oxidation b. $[Fe_2O(bpy)_4Cl_2]^{3+}$ reduction c. Colors of spectra roughly correspond to the solution of the three species.

3.3.2 Bulk electrolysis of high concentration catholyte

$Fe(bpy)_3^{3+}$ has a very light blue color (molar absorptivity smaller than $Fe(bpy)_3^{2+}$), thus it is difficult to collect the peak absorbance of this species at low concentration. However, UV-Vis cannot detect sample at concentrations that are too high; therefore, the tested solution that contain 0.025M $Fe(bpy)_3SO_4$ was prepared to satisfy both requirements. At this concentration, the long wavelength feature of $Fe(bpy)_3^{3+}$ (627 nm) could be resolved during the bulk electrolysis; its appearance/disappearance over the duration of the experiment corresponds to the generation/dimerization of this species, respectively. The control solution without additives was 0.025 M $Fe(bpy)_3SO_4$ in 1 M NaCl. Other tested solutions had the similar condition but with the addition of 1 M additives, similar to the UV-vis study above.

To evaluate the dimerization process of $Fe(bpy)_3SO_4$, $Fe(bpy)_3^{2+}$ was only fully oxidized by BE at 1.2V (no reduced back), which is analogous to the charging phase in an RFB. We expect that the concentration of $Fe(bpy)_3^{3+}$ would reach a maximum at some point and then decrease due to dimerization. The original $Fe(bpy)^{2+}$ solution has a red color, which absorb in the green region (490nm-560nm), and $Fe(bpy)_3^{3+}$ solution has blue color, which absorbs in the orange region (580nm-630nm). Therefore, we will study the $Fe(bpy)_3^{3+}$ absorbance at the long wavelength, especially the peak at 610nm. The absorbances were recorded during and after electrolysis @627nm (Figure 3.12). At the beginning, the peak @627nm, which is considered as concentration of $Fe(bpy)_3^{3+}$, increase during electrolysis ($Fe(bpy)_3^{2+}$ is oxidized). Then it starts to decrease after nearly reach 1.00. Figure 3.13 shows the absorbance of $Fe(bpy)_3^{3+}$ versus time @627nm. The absorbance reach maximum around 1500s during the oxidation before the electrolysis stop at 2000s, which represent equation (1). Then the absorbance keeps decreasing until 8400s due to the dimerization process (equation (2)). The slope of absorbance from 1500s to 8400s was considered

as the dimerization rate of $Fe(bpy)_3SO_4$. The spectra below 600nm have high absorbance at the beginning due to the presence of $Fe(bpy)_3^{2+}$ and we only see the edge of its absorbance band, which decrease during electrolysis as the 610 nm peak of febpy3+ emerges. The $Fe(bpy)_3^{2+}$ absorbance around 500 nm somewhat recovers after electrolysis. For these experiments, the absorbance at 627 nm will be tracked, where the greatest difference between $Fe(bpy)_3^{2+}$ and $Fe(bpy)_3^{3+}$ features can be distinguished.

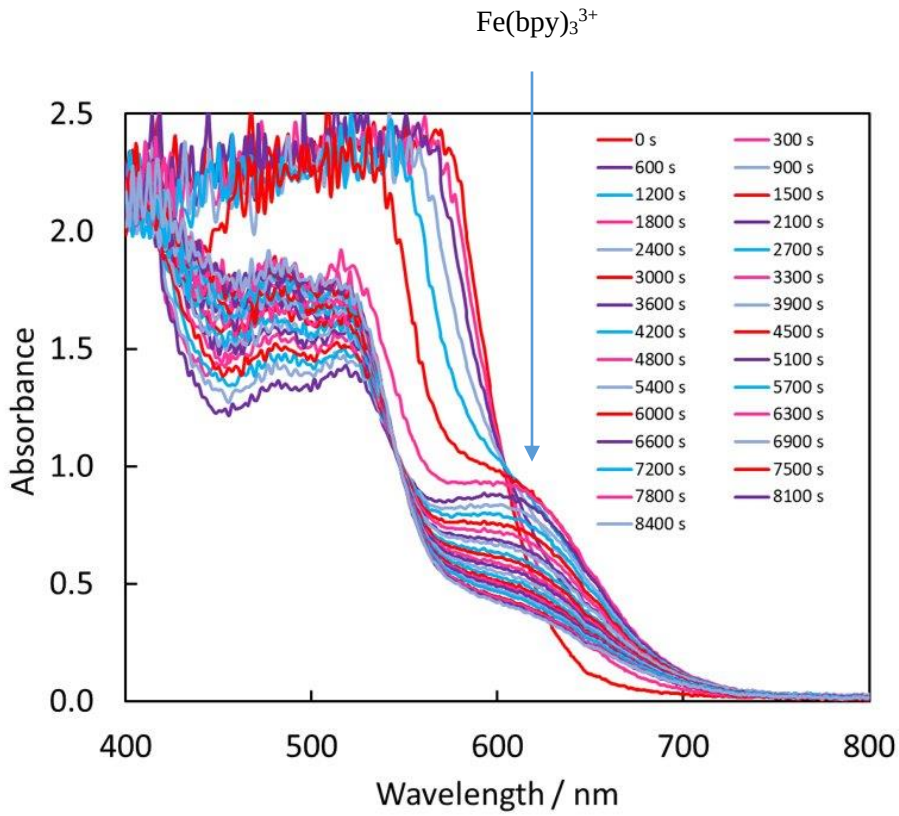

Figure 3.12 UV-Vis absorption spectra of 0.0.25M $Fe(bpy)_3SO_4$ in 1M NaCl during electrolysis (fully oxidized) that focuses on changes around the absorbance feature of $Fe(bpy)_3^{3+}$ at 610nm.

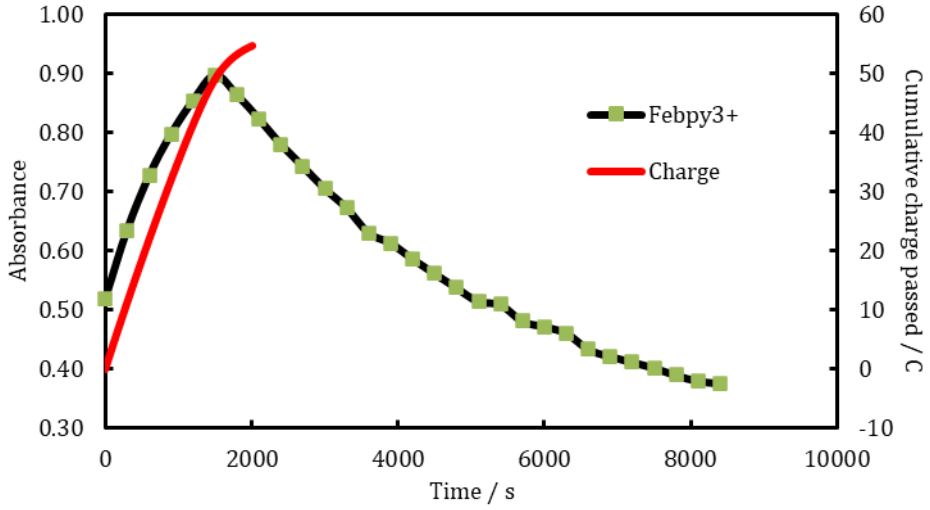

Figure 3.13 Electrolysis and absorbance of 0.025M $Fe(bpy)_3SO_4$ in 1M NaCl versus time

The BE experiment at high concentration repeated with different additives to collect the dimerization rate of $Fe(bpy)_3^{3+}$. From computational studies, $NaSO_4$ and NaF were identified as potential species that could inhibit dimerization (i.e. dimers containing F or SO_4 ligands were computed to be less favored than the Cl-based dimer). Moreover, NaF was also favorable for increasing the solubility of $Fe(bpy)_3SO_4$. However, the experimental BE results yielded a precipitate formed during electrolysis in both cases. Thus, all other additive tests remained in NaCl as the supporting electrolyte. As with the solubility study, additives were rationally chosen so that they might inhibit/disrupt the chemistry of equation 3.

The dimerization rate of the control and additive solutions are show in Table 3. The dimerization rate was determined by the same as the control. By comparing the dimerization rate of $Fe(bpy)_3^{3+}$ in different additives to the control, there were three additives that slowed the dimerization rate: IPA, Ethylene glycol (EG) and Glycerol (GC). Polyethylene glycol (PEG) appear to give the lowest dimerization rate; however, the absorbance peak of $Fe(bpy)_3^{3+}$ @ 610nm

never reach as high as the control. This observation suggests that the dimerization process even proceeds faster in the presence of PEG.

Since it also worked well for improving solubility of $Fe(bpy)_3^{2+}$ we decided to focus on the 1 M IPA additive. Figure 3.14 illustrate the absorbance of $Fe(bpy)_3^{3+}$ versus time for the control and IPA solutions. According to Beer's Law, increasing of absorbance means the increasing in concentration of $Fe(bpy)_3^{3+}$. As expected, the concentration of $Fe(bpy)_3^{3+}$ increasing and then decreasing after 1500s for the control solution and 2100s for IPA solution due to the attack of water and ensuing dimerization reaction. As indicated in the figure, the dimerization rate was estimated by the slope of absorbance loss after 1500s and 2100s. The dimerization rate of IPA was slightly lower than the control solution; however, the peak of $Fe(bpy)_3^{3+}$ was shifted to the right for IPA solutions (Figure 3.14), which means that the $Fe(bpy)_3^{3+}$ species were formed slower than the control solution. This behavior suggests that the kinetics of oxidation are somewhat more sluggish with the IPA additive but that the dimerization rate may also be suppressed. This behavior will be further clarified in the battery tests discussed below. Figure 3.15 show the current/charge of $Fe(bpy)_3^{2+}$ with and without 1 M IPA additive. As the absorbance of $Fe(bpy)_3^{2+}$ shift to the right (Fig 3.14), the current and charge of solution with 1 M IPA additive are also shift to the right.

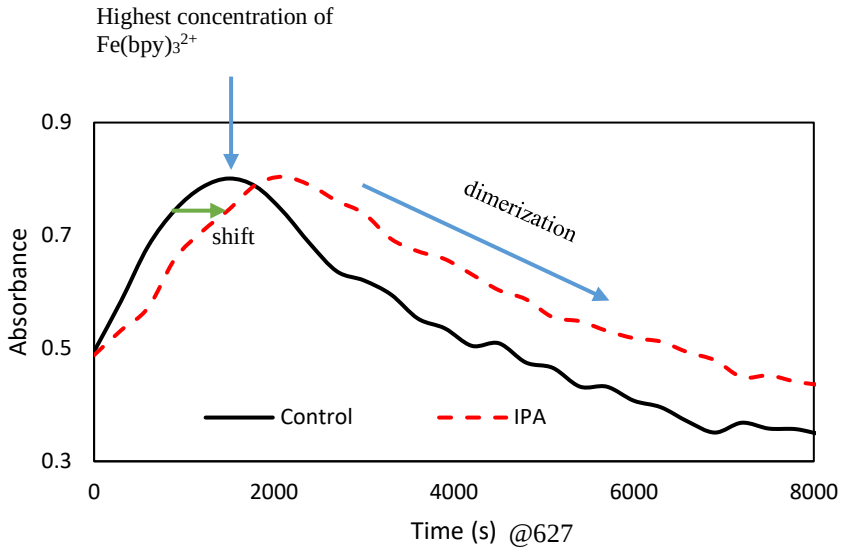

Figure 3.14 The absorbance of 0.025 M $Fe(bpy)_3^{3+}$ versus time with and without 1 M IPA

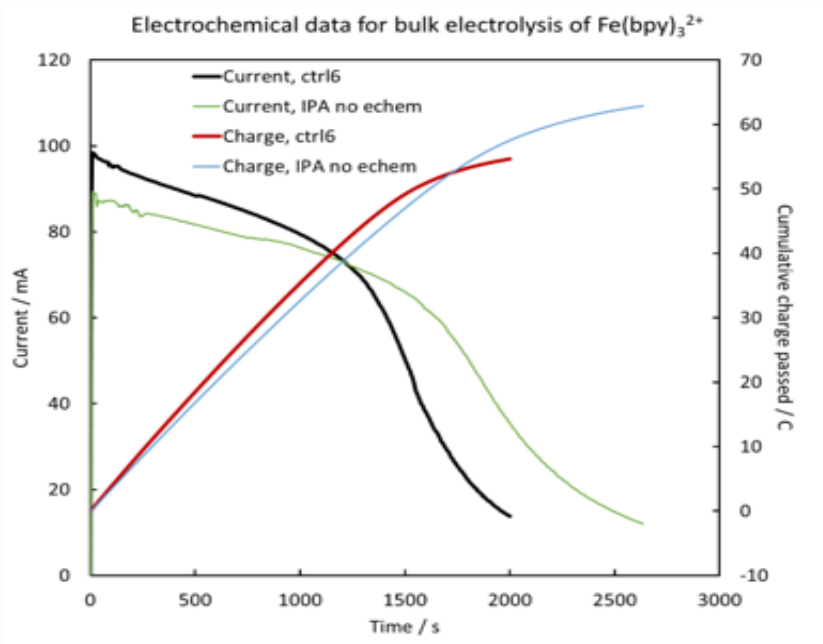

Figure 3.15 Electrochemical data for bulk electrolysis of $Fe(bpy)_3^{2+}$ with and without 1 M IPA additive.

Supporting electrolyte	Additives	Dimerization rate ($M/s * 10^{-5}$)
1M NaCl	N/A	-6.31
1M NaCl	1M Isopropyl	-6.15
1M Na_2SO_4	N/A	Brown precipitate
1M NaCl	1M Ethylene glycol	-6.13
0.9M NaF	N/A	White precipitate
1M NaCl	0.45M Sodium xylene	-7.10
1M NaCl	0.1M PolyEthylene Glycol	-5.61
1M NaCl	1M Glycerol	5.85

Table 3. Dimerization rate of $Fe(bpy)_3^{3+}$ with different salt and additives.

3.4. Effect of IPA on Iron – Complex

3.4.1 Cyclic Voltammetry

To gain further insight on how IPA might ultimate affect battery performance, the electrochemical tests for the control solution from Section 3.1 above were repeated for the IPA additive solution. The solution was 4 mM $Fe(bpy)_3SO_4$ in 1M NaCl plus 1 M IPA solution. The result in Figure 3.16 showed that the complex still displays reversible behavior, very similar to the control. There is no change in peak separation, which is ~65mV. Nevertheless, the peaks were shifted up to the right by a small amount that will not have a big impact on its electrochemical performance. The redox potential (center between two peaks) shifts from 0.85V (without IPA) to 0.87V (with IPA).

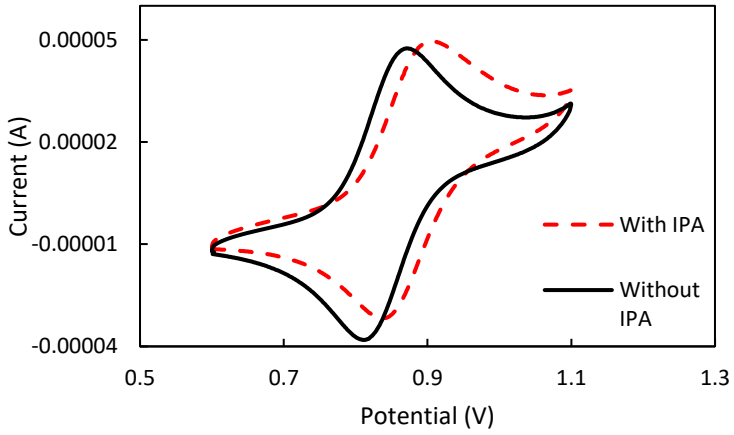

Figure 3.16 The cyclic voltammogram of 4mM $Fe(bpy)_3SO_4$ in 1M NaCl and 1M IPA at 50 mV/s on a glassy carbon working electrode.

3.4.2 Kinetic studies

Since IPA can increase the solubility of $Fe(bpy)_3SO_4$ up to ~0.35M in NaCl, the electrochemical kinetic study was also carried out to investigate the effect of IPA on the diffusion

coefficient and electron transfer rate of the iron – complex. The LSV was performed with 4mM $Fe(bpy)_3SO_4$ in 1M NaCl and 1M IPA at scan rate 10mV/s with potential range from 0.7V to 1.0V, and at different rotation rate ranging from 300rpm to 3000rpm.

a

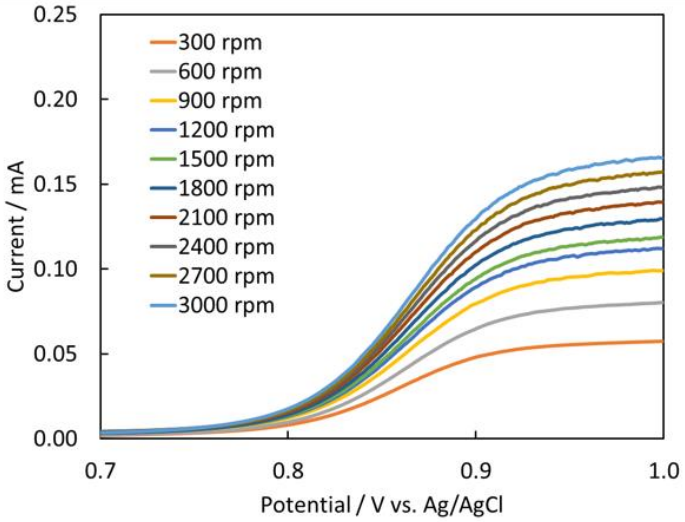

b

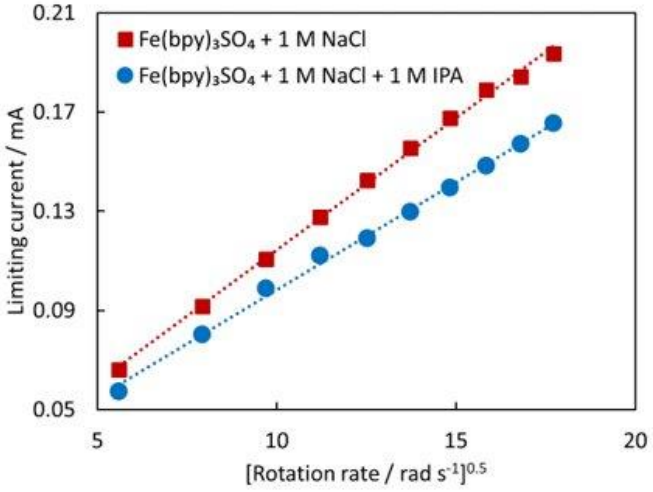

Figure 3.17 The kinetic study of 4mM $Fe(bpy)_3SO_4$ in 1M NaCl and 1M IPA. (a) linear sweep voltammogram at scan rate 10mV/s. (b) Levich plot of the $Fe(bpy)_3SO_4$ solution with and without IPA.

Figure 3.17 showed the result of LSV and Levich plot of the control and additive solutions. The diffusion coefficient and transfer rate constant of $Fe(bpy)_3SO_4$ with IPA was calculated to be 1.61 x 10^{-6} cm^2/s and 2.82 x 10^{-2} cm/s, which is somewhat lower than the diffusion coefficient (2.08 x 10^{-6} cm^2/s) and transfer rate constant (3.2 x 10^{-2} cm/s) of $Fe(bpy)_3SO_4$ without IPA. However, the difference was small, and it should severely affect the performance of $Fe(bpy)_3SO_4$ in the battery.

3.4.3 Battery performance

3.4.3.1 Cycling and power output

To evaluate the effect of IPA on the performance of a $Fe(bpy)_3SO_4$ based battery, a lab scale RFB was constructed with 0.1M $Fe(bpy)_3SO_4$ in 1 M KCl and 1 M IPA serving as catholyte (test solution), and 0.15M AQDS in 1M KCl serve as anolyte. The battery cell was set up and operated under the same conditions as the control battery.

a

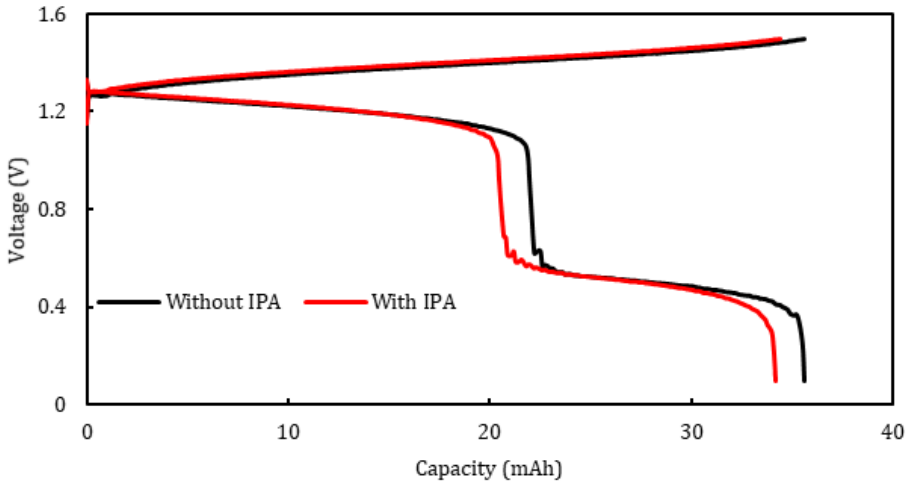

b

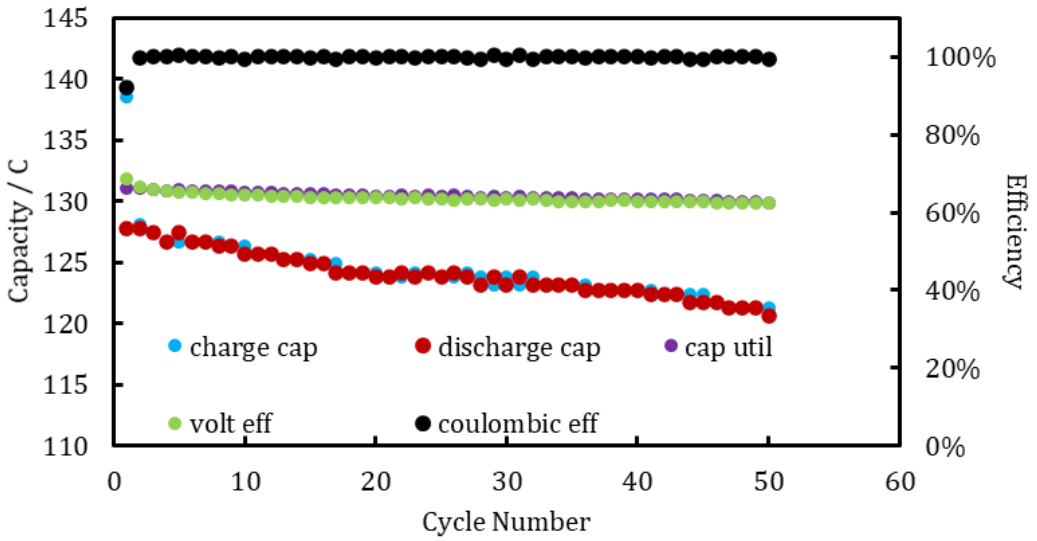

c

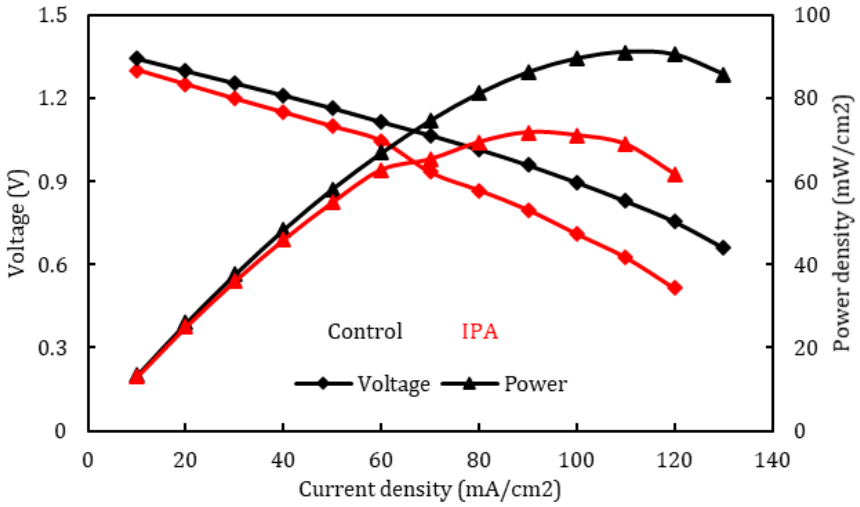

Figure 3.18 The battery performance of $Fe(bpy)_3SO_4$ and AQDS in 1M KCl and 1M IPA. (a)Charge – discharge of 30th cycle at current density of 20mA/cm^2 with and without IPA (b) Cycling performance with IPA includes efficiency and capacity. (c) Cell voltage and power density curves.

In general, the performance of the batteries with and without IPA were similar to each other (Figure 3.18 (a)). The battery cell provided an open circuit of 1.25V that in agreement with CV. It delivered 74% of theoretical capacity and still have a low voltage and energy efficiency due to dimerization, which will be discussed later. The capacity that the battery cell with IPA delivered was somewhat smaller than without IPA; consistent with the RDE results; again, it was a small amount and the Coulombic efficiency of the battery was still very high, around 99.7%. The trend of coulombic efficiency, voltage efficiency and capacity utilization shown in Figure 3.18 (b). The loss in capacity can come from the effect of oxygen on negative side, slightly variation in battery set up, effect of IPA, or membrane crossover. The control capacity fade was 0.14%/cycle while the IPA battery showed 0.09%/cycle. The energy densities achieved were 12.0 Wh/L for the control and 11.2 Wh/L for the IPA additive battery. The power curve of the battery without IPA shows a higher peak output than with IPA (90mW/cm^2 and 71mW/cm^2, respectively) (Figure 3.18c). The peak of power curve in the control is delivered at a current density of 120mA/cm^2, and for the IPA additive battery it is 100mA/cm^2. The different between control and IPA might because of lower diffusion coefficient and electron transfer rate constant of the IPA compared to the control. Table 4 summarize all the different parameters between the control and IPA solution. Although adding IPA does not have any significant changes on battery performance, it reduced the capacity fade rate. This means it reduce the capacity loss between each cycle, which is a huge effect. The data was only recorded for one time; therefore, the battery performance will be tested more in the future to have a better conclusion.

	Without 1 M IPA	With 1 M IPA
Coulombic efficiency	99.7%	99.7%
Voltage efficiency	65.2%	63.7%
Energy efficiency	65.0%	63.5%
Capacity utilization	67.4%	64.3%
Capacity fade rate	0.14%	0.09%
Power density	90mW/cm^2	71mW/cm^2
Peak of power curve	120mA/cm^2	100mA/cm^2
Energy density	12.0 Wh/L	11.2 Wh/L

Table 4. Comparison of different metric of 0.1 M $Fe(bpy)_3SO_4$ and 0.15 M AQDS in 1 M NaCl with and without IPA.

3.4.3.2 Dimerization study

Since the battery performance did not have any major changes with the solubility enhancing additive, we now focus on analyzing the dimerization process. Figure 3.19 shows the monomer capacity, dimer capacity and percentage of dimerization between the control and additive catholytes. The monomer capacity of the IPA solution is lower than the control solution, but the dimer capacity stays the same which result in the higher in percentage of dimerization.

These results agree with the bulk electrolysis experiment, where it took more time to reach the highest concentration of $Fe(bpy)_3^{3+}$ in the tested solution; nevertheless, the dimerization rate was about the same. At the beginning the monomer capacity gap was 15 C, then the gap narrowed down to 5 C (Figure 3.19 a). As we can see, the monomer capacity of the control solution was

decreasing faster than the monomer capacity of tested solution. Overall, adding IPA into the catholyte does not appear to significantly affect dimerization in the battery under these conditions.

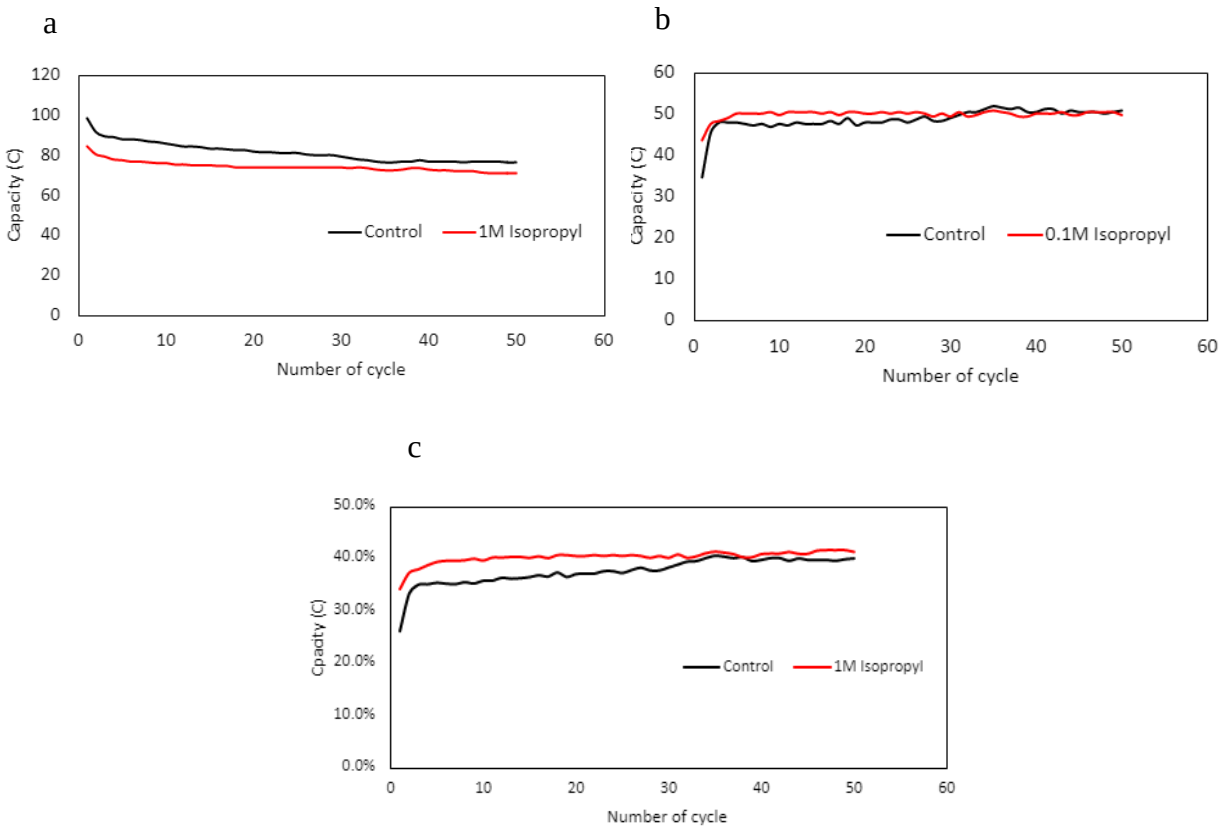

Figure 3.19 The comparison between (a). monomer capacity (b). dimer capacity (c) percentage of dimerization of an AQDS – $Fe(bpy)_3SO_4$ RFB with and without 1 M IPA catholyte additive.

To investigate how fast the dimer will form, we programmed the battery to rest between charge and discharge steps. We expected that the longer the battery rests, the more dimers would form. We programmed the Landt Instrument to allow the battery to fully charged then rest at open circuit for 15mins before discharge. Then normal cycling (no rest phase) for 3 cycles. The same process was applied for 30 mins, 45 mins and 60 mins rest phases. As expected, the most dimer

was formed (measured as dimer capacity and % dimerization) after 60 mins of rest and least in 15 mins of rest (Figure 3.20a). After 60 mins of rest, the charged catholyte had almost completely converted to the dimer form and very few monomers were left. The trend of monomer capacity, dimer capacity and percentage of dimerization were illustrated in Figure 3.20b. The four sharp peaks of monomer capacity and dimer capacity represent for 15mins, 30mins, 45mins and 60mins of rest, where the flat lines are the normal cycling, which recovered to normal behavior. The peaks of monomer capacity are symmetric with dimer capacity, which means the amount of monomer that decreasing equal to the amount of dimer that increasing. The percentage of dimerization are 70%, 81%, 90% and 96% for 15mins, 30mins, 45mins and 60mins of rest, respectively. There is no change in the voltage drop between monomer and dimer. Although the dimer formed during the rest, they were able to be reduced back during discharge. The coulombic efficiency is around 99.8%. These results show that voltage loss due to dimerization occurs rapidly if a battery is held in the 100% charge state for any amount of time. A practical RFB will be expected to hold its charge over many hours or even days, thus a new strategy to prevent dimerization should be explored in order to maximize voltage efficiency in a $Fe(bpy)_3SO_4$-based battery.

a

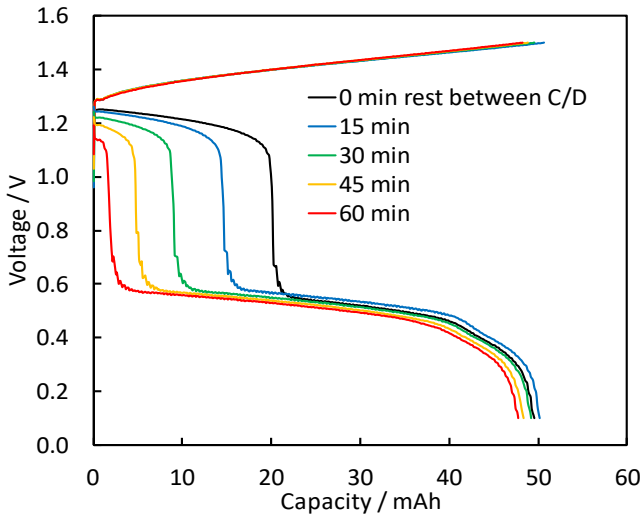

b

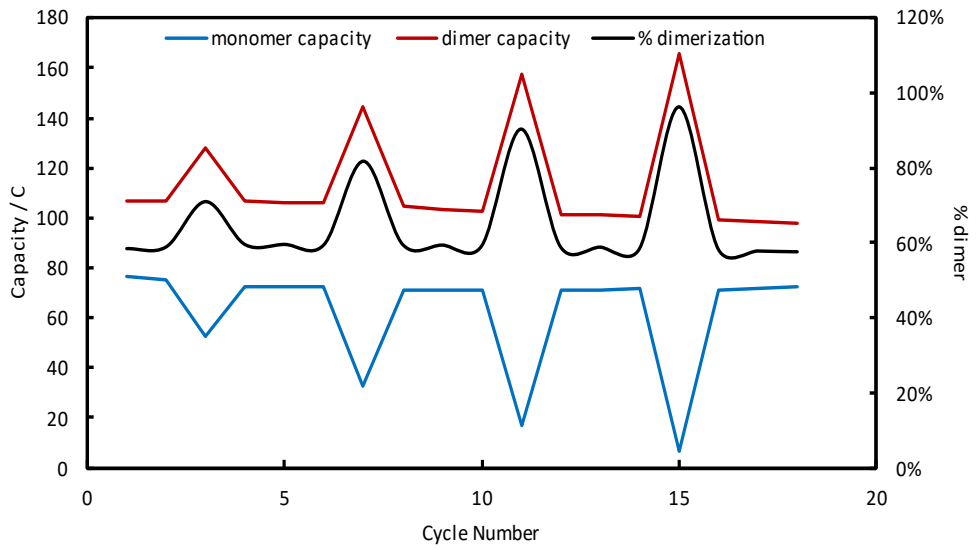

Figure 3.20 Battery performance of 0.15M $Fe(bpy)_3SO_4$ in 1M KCl and 1M IPA (a) the charge – discharge cycle at different rest. (b) the trend of monomer capacity, dimer capacity and percentage of dimerization over 18 cycles.

3.5. Battery performance with high concentration catholytes

Since IPA can increase the solubility of $Fe(bpy)_3SO_4$, we increased the concentration of the active species to different concentrations, including 0.15 M, 0.2 M and 0.25 M, to investigate its behavior under otherwise similar conditions. The only thing different is the concentration of the catholyte active species in each battery. The catholyte and anolyte supporting electrolyte is 1 M KCl plus 1 M IPA in to achieve the higher concentration batteries.

There is no change in performance of catholyte at different concentrations during the charge cycle aside from the greater capacity, as expected. However, we can see differences in the discharge data (Figure 3.21). Although the two plateaus are still present at different concentrations, the monomer capacity is about the same level for all the concentration and

only the dimer capacity increases with concentration (showed in Figure 3.21a). The voltage efficiency and energy efficiency are lower at the high concentration battery. The Coulombic efficiency is around 99.8% for all concentrations studied indicating no irreversible side reactions occur. The open circuit voltage is also the same as other batteries at 1.25V. Thus, we can conclude that increasing the catholyte concentration means increasing dimer while the monomer concentration (capacity) is constant. The trend of dimerization was showed very clearly in Figure 3.21b. The percentage of dimerization stays around 35% for 0.1 M, then 50% and 70% for 0.15 M and 0.2 M, respectively. Figure 3.21c shows the dimerization percentage versus different concentration of $Fe(bpy)_3SO_4$, which increasing concentration is increasing dimerization percentage. A battery using 0.25 M $Fe(bpy)_3SO_4$ was tested, however precipitation, possibly of $Fe(bpy)_3^{3+}$, was observed during charge – discharge cycling (Figure 3.23). Therefore, we decided to use 0.2 M of Iron – complexes in the catholyte as the highest concentration in the battery performance for subsequent long-term cycling tests of the $Fe(bpy)_3SO_4$/AQDS RFB.

Figure 3.22 shows the power curves and voltage of the 0.10 M, 0.15M and 0.2 M $Fe(bpy)_3SO_4$ under identical conditions. All three batteries gave the highest peak power density at current density of 120 mA/cm2. Nevertheless, the power density of the lower concentration is higher than for 0.15 M and 0.20 M. The peak power density of 0.10 M, 0.15M and 0.2M are 90.4mW/cm^2, 82.4mW/cm^2 and 85.5mW/cm^2, respectively. The reason why power density is lower at higher concentration might because of faster dimerization, lower diffusion coefficient, lower transfer rate, etc. Further effects of IPA on battery will be studied deeply in the future such as adding redox targeting compound that is promising to overcome the solubility and maybe dimerization process.

a

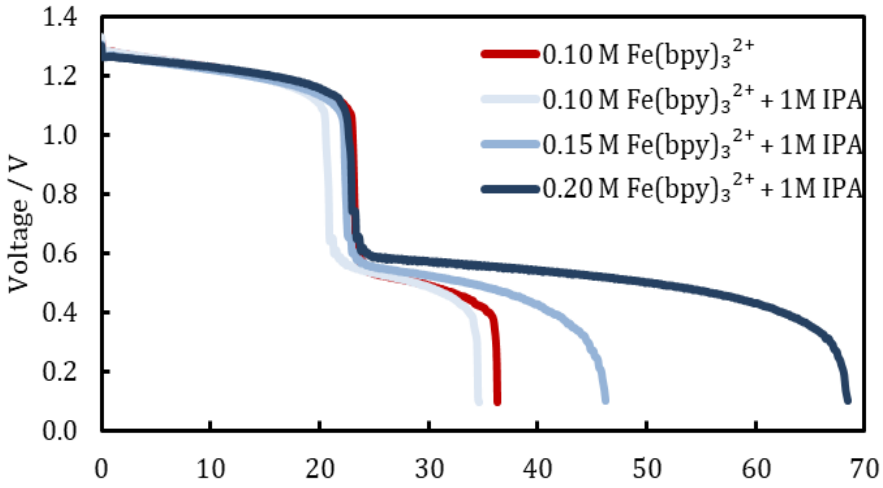

b

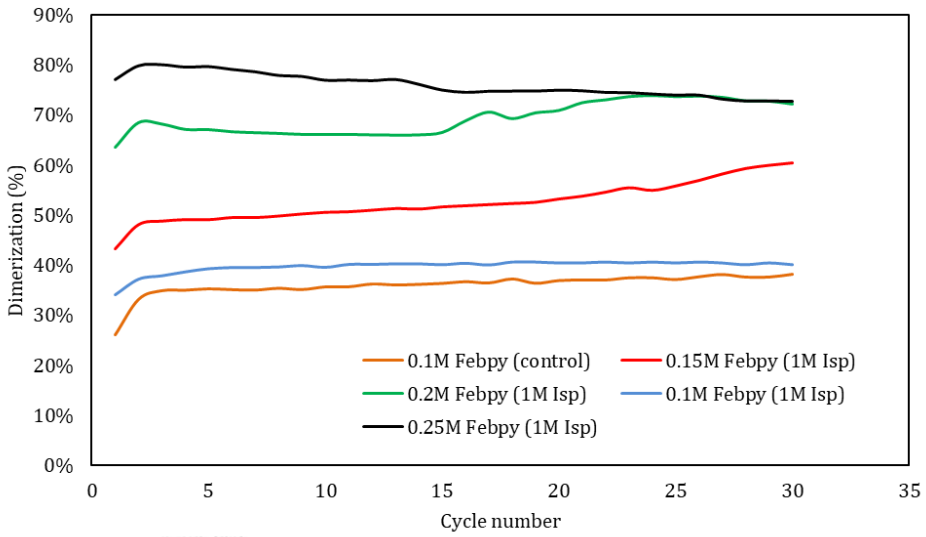

c

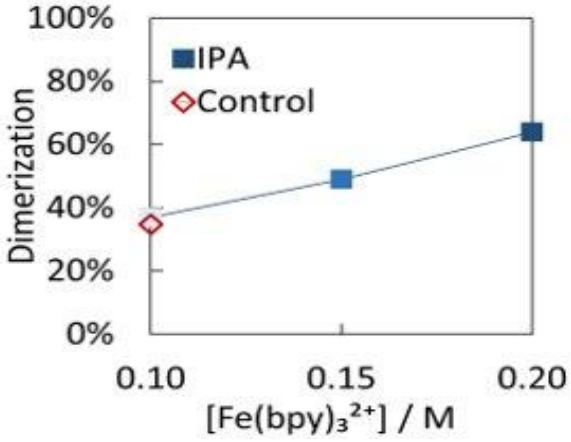

Figure 3.21 Battery performance of high – concentration catholytes (with 1 M IPA additive) at 0.10 M, 0.15 M, 0.20 M Fe(bpy)3SO4 a. Discharge cycle (15^{th} cycles shown) of different

concentrations of the catholyte b. Percentage of Dimerization at different concentration. c. Dimerization of the control and IPA

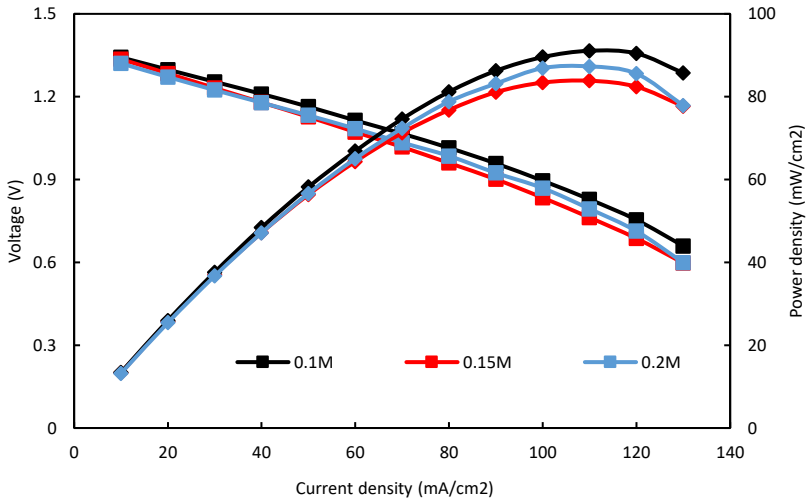

Figure 3.22 Voltage and power density of 0.10 M, 0.15 M and 0.20 M $Fe(bpy)_3SO_4$.

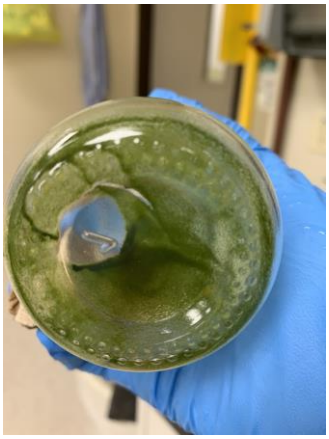

Figure 3.23 Precipitation in 0.25 M $Fe(bpy)_3SO_4$ battery.

The dimerization process was further investigated at different SOC. This is an important aspect, which help describing the actual energy level available of the battery [29]. We charged the battery at different cut off voltage: 1.7V, 1.6V, 1.5V and 1.4V (Fig 3.23a). We assumed that it is

100% state of charge (SOC) at 1.7V due to the sharp curve at the end of charging state. The open circuit of the battery is decrease and voltage drop is increase when the SOC decrease. Both monomer capacity and dimer capacity are decreasing. However, Figure 3.24 shows the dimerization rate that decreasing when SOC increasing.

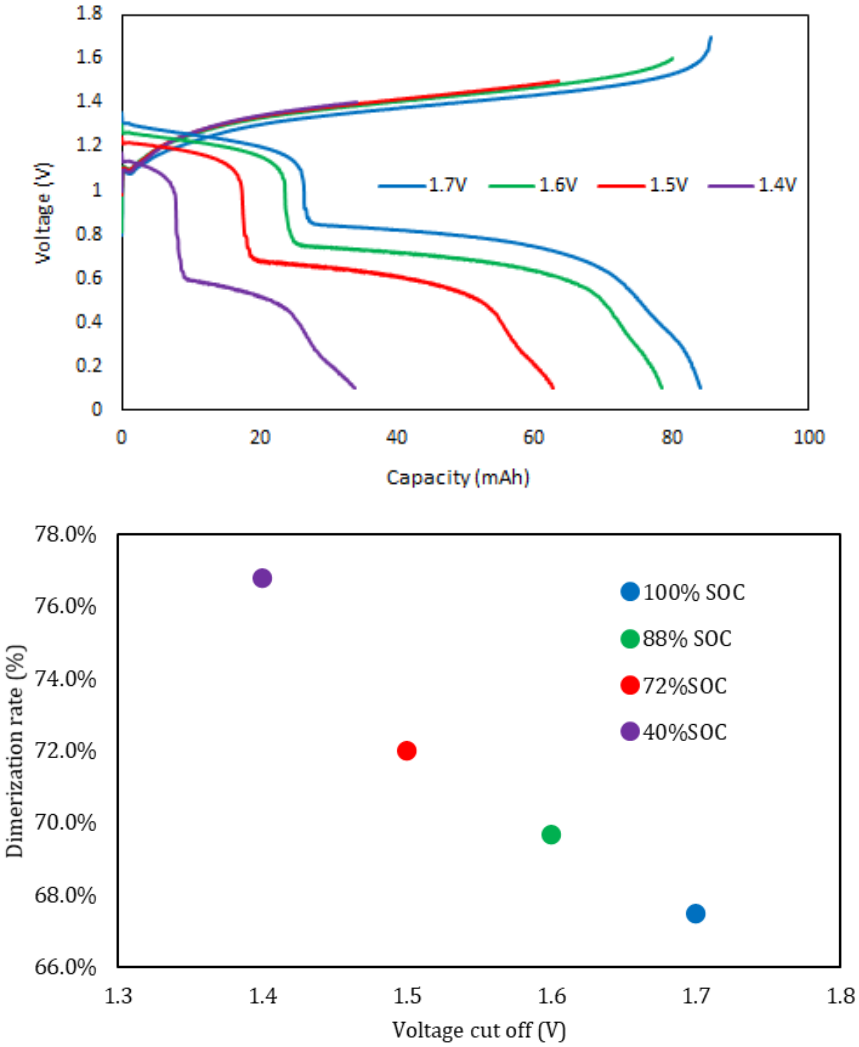

Figure 3.24 Different state of charge of 0.2 M $Fe(bpy)_3SO_4$ in 1 M KCl solution

CHAPTER IV – CONCLUSION

4.1. Summary

In summary, we carried out a thorough study on the additive IPA that was discovered to enhance the solubility of $Fe(bpy)_3SO_4$, a promising low-cost catholyte for aqueous redox flow batteries that operate under near-neutral pH conditions. Adding IPA into the supporting electrolyte increases the solubility of $Fe(bpy)_3SO_4$ from 0.10 M up to 0.35 M. $Fe(bpy)_3SO_4$ with the additive still showed reversible electrochemical behavior and kinetics in 1M NaCl and 1 M IPA, comparable to the control solution. On the other hand, dimerization process was studied deeper for the first time by using BE with *in situ* UV-Vis probing. Despite the enhancement in solubility, IPA gave a similar dimerization rate to the control. Different additives were also studied to increase solubility and prevent dimerization such as, ethylene glycol, sodium xylenesulfonate, etc. which should be investigate further in the future.

For the first time, 2,6-AQDS and $Fe(bpy)_3SO_4$ were used to build an RFB. The open circuit for this redox couple is among the highest for aqueous RFBs at 1.30V and the peak power density is 120mW/cm^2. The battery performance was stable and gave a high coulombic efficiency. However, there is still a loss in voltage due to the dimerization process, which also leads to low energy efficiency; this problem will need to be addressed before $Fe(bpy)_3SO_4$ -based batteries can be commercially competitive with vanadium RFBs currently on the market. Combining with IPA, we built a battery with the highest $Fe(bpy)_3SO_4$ concentration demonstrated to date, with successful operation at 0.15 M and 0.20 M in 1 M KCl and 1 M IPA. Despite the good capacity (70 mAh or 3.5 Ah/L) of the highest concentration, its dimer capacity is increases instead of the monomer capacity, which remains constant at all catholyte concentrations. This is the reason why high concentration has lower voltage efficiency and energy

efficiency. However, the coulombic efficiency is still nearly 100% and the peak power density is 120mW/cm^2, which higher than some publish ARFBs (i.e 91.5mW/cm^2 of AQDS$(NH_4)_2$/NH_4I [30], or 100mW/cm^2 of FcNCl/MV [31])

4.2. Future work

In this study, the effect of IPA on solubility, dimerization and battery performance was studied. The solubility of $Fe(bpy)_3SO_4$ was improved by IPA but not the dimerization issue. These results help us to understand better on $Fe(bpy)_3SO_4$ – based catholytes for aqueous RFBs. Future work that should be performed to further improve this catholyte's performance is:

- Investigating deeper the effect of IPA on the battery performance. The main reason why adding IPA in the solution will reduce monomer capacity and the performance of $Fe(bpy)_3SO_4$/AQDS RFB.
- Although IPA increasing the solubility of $Fe(bpy)_3SO_4$ in 1 M KCl solution, IPA did not improve the performance. There are many other additives can be tested to further improve solubility and reduce dimerization.
- If IPA increases the solubility of $Fe(bpy)_3SO_4$, it may also increase the solubility of the AQDS anolyte in 1 M KCl; the effects of anolyte performance with IPA additive should be studied as well.
- Improving the capacity of the $Fe(bpy)_3SO_4$/AQDS RFB by adding redox targeting to the catholyte (and anolyte). A promising redox material is CuHCF, which has a similar redox potential to $Fe(bpy)_3SO_4$.

REFERENCES

[1] Z. Yang et al., “Electrochemical Energy Storage for Green Grid,” Chem. Rev., vol. 111, no. 5, pp. 3577–3613, May 2011.

[2] S. Smith, M. Clark, T. Fairbanks, T. Prinzi, K. Delgado, “Nuclear power – Pros and Cons”.

[3] Nguyen, T., & Savinell, R. F. (2010). Flow Batteries. The Electrochemical Society Interface, 19(3), 54–56.

[4] Vanýsek, P., & Novák, V. (2017). Redox flow batteries as the means for energy storage. Journal of Energy Storage, 13, 435–441.

[5] Emmett, R. K.; Roberts, M. E., Recent developments in alternative aqueous redox flow batteries for grid-scale energy storage. *J. Power Sources* **2021,** *506*.

[6] Chakrabarti, M.h., et al. “Evaluation of Electrolytes for Redox Flow Battery

[7] Yang, B., Hoober-Burkhardt, L., Wang, F., Surya Prakash, G. K., & Narayanan, S. R. An Inexpensive Aqueous Flow Battery for Large-Scale Electrical Energy Storage Based on Water-Soluble Organic Redox Couples. *Journal of The Electrochemical Society* (2014).

[8] DeBruler, C., Hu, B., Moss, J., Liu, X., Luo, J., Sun, Y., & Liu, T. L. (2017). Designer Two-Electron Storage Viologen Anolyte Materials for Neutral Aqueous Organic Redox Flow Batteries.

[9] Ruan, W., Mao, J., Yang, S., & Chen, Q. (2020). Communication—Tris(bipyridyl)iron Complexes for High-Voltage Aqueous Redox Flow Batteries. *Journal of the Electrochemical Society*.

[10] Hendriks, K. H.; Robinson, S. G.; Braten, M. N.; Sevov, C. S.; Helms, B. A.; Sigman, M. S.; Minteer, S. D.; Sanford, M. S. High- Performance Oligomeric Catholytes for Effective Macromolecular Separation in Nonaqueous Redox Flow Batteries. *ACS Cent. Sci*. 2018, 4, 189−196.

[11] Xing, W., Yin, G., Zhang, J. Rotating Electrode Methods and Oxygen Reduction Electrocatalysis; Elsevier, 2014; p.171-198.

[12] Chen, Y., Xu, Z., Wang, C., Bao, J., Koeppel, B., Yan, L., … Wang, W. (2021). Analytical modeling for redox flow battery design. *Journal of Power Sources.*

[13] Wang, H.; Sayed, S. Y.; Luber, E. J.; Olsen, B. C.; Shirurkar, S. M.; Venkatakrishnan, S.; Tefashe, U. M.; Farquhar, A. K.; Smotkin, E. S.; McCreery, R. L.; Buriak, J. M., Redox Flow Batteries: How to Determine Electrochemical Kinetic Parameters. *ACS Nano 2020.*

[14] Hendriks, K. H.; Robinson, S. G.; Braten, M. N.; Sevov, C. S.; Helms, B. A.; Sigman, M. S.; Minteer, S. D.; Sanford, M. S. High- Performance Oligomeric Catholytes for Effective Macromolecular Separation in Nonaqueous Redox Flow Batteries. *ACS Cent. Sci. 2018*, 4, 189−196.

[15] Xiao, J., Li, Q., Bi, Y. et al. Understanding and applying coulombic efficiency in lithium metal batteries. *Nat Energy* **5,** 561–568 (2020).

[16] Eftekhari, A. (2017). Energy efficiency: a critically important but neglected factor in battery research. Sustainable Energy & Fuels, 1(10), 2053–2060.

[17] Xie, Z., Wei, L. & Zhong, S. An aqueous $ZnCl_2$/$Fe(bpy)_3Cl_2$ flow battery with mild electrolyte. Front. Mater. Sci. **14,** 442–449 (2020).

[18] Mun, J., Lee, M.-J., Park, J.-W., Oh, D.-J., Lee, D.-Y., & Doo, S.-G. (2012). Non-Aqueous Redox Flow Batteries with Nickel and Iron Tris(2,2′-bipyridine) Complex Electrolyte. Electrochemical and Solid-State Letters, 15(6), A80.

[19] Chen, Y. W. D., Santhanam, K. S. V., & Bard, A. J. (1981). Solution Redox Couples for Electrochemical Energy Storage: I. Iron (III)-Iron (II) Complexes with O-Phenanthroline and Related Ligands. *Journal of the Electrochemical Society*, 128(7), 1460.

[20] Ehman. "Electrochemistry and Hydrolysis Kinetics of the 2,2'-Bipyridine Complexes of iron(III) and iron(II)." Inorganic Chemistry., vol. 8, no. 4, American Chemical Society, 1969, pp. 900-03.

[21] Friedrich, J. M., Ponce-de-León, C., Reade, G. W., & Walsh, F. C. (2004). Reticulated vitreous carbon as an electrode material. *Journal of Electroanalytical Chemistry*, 561, 203-217.

[22] Liu, B., Tang, C., Jiang, H., Jia, G., & Zhao, T. (2020, October 06). An aqueous organic redox flow battery employing a trifunctional electroactive compound as anolyte, catholyte and supporting electrolyte. *Journal of Power Sources*.

[23] Epifanio M, Inguva S, Kitching M, Mosnier JP, Marsili E. Effects of atmospheric air plasma treatment of graphite and carbon felt electrodes on the anodic current from Shewanella attached cells. *Bioelectrochemistry*. 2015 Dec;106(Pt A):186-93.

[24] Rupak Banerjee, Nico Bevilacqua, Arezou Mohseninia, Benjamin Wiedemann, Florian Wilhelm, Joachim Scholta, Roswitha Zeis. Carbon felt electrodes for redox flow battery: Impact of compression on transport properties. *Journal of Energy Storage*, Volume 26, 2019.

[25] Lee, W., Permatasari, A., & Kwon, Y. (2020). Neutral pH aqueous redox flow batteries using anthraquinone-ferrocyanide redox couple. *Journal of Materials* Chemistry C.

[26] Lee, W., Permatasari, A., Kwon, B. W., & Kwon, Y. (2019). Performance evaluation of aqueous organic redox flow battery using anthraquinone-2,7-disulfonic acid disodium salt and potassium iodide redox couple. *Chemical Engineering Journal*, 358, 1438–1445.

[27] Hu, B., DeBruler, C., Rhodes, Z., & Liu, T. L. (2017). Long-Cycling Aqueous Organic Redox Flow Battery (AORFB) toward Sustainable and Safe Energy Storage. *Journal of the American Chemical Society*, 139(3), 1207–1214.

[28] X. Zu, L. Zhang, Y. Qian, C. Zhang, G. Yu, Angew. Chem. Int. Ed. **2020**, 59, 22163.

[29] Ogura, K., & Kolhe, M. L. (2017). Battery technologies for electric vehicles. Electric Vehicles: Prospects and Challenges, 139–167.

[30] Hu, B., Luo, J., Hu, M., Yuan, B., & Liu, T. L. (2019). A pH Neutral, Metal Free Aqueous Organic Redox Flow Battery Employing an Ammonium Anthraquinone Anolyte. Angewandte Chemie.

[31] Ding, Y., & Yu, G. (2017). The Promise of Environmentally Benign Redox Flow Batteries by Molecular Engineering. Angewandte Chemie International Edition, 56(30), 8614–8616